Department of Physics and Astronomy

University of Heidelberg

Master thesis
in Physics

submitted by
Maxime Joos
born in Paris

2013

Phase contrast imaging of

mesoscopic Bose-Einstein condensates

This master thesis has been carried out by **Joos Maxime** at the

Kirchhoff-Institute for Physics

under the supervision of
Prof. M. K. Oberthaler

Danksagung

Phasenkontrastabbildung mesoskopischer Bose-Einstein-Kondensate

Wir untersuchen theoretisch und experimentell die Eigenschaften des Phasenkontrastverfahren für die Beobachtung mesoskopischer Bose-Einstein-Kondensate aus ^{87}Rb Atome. Wir betrachten insbesondere einen unerforschten Bereich, in dem der Abbildungsstrahl nah-resonant ist und den atomaren Übergang sättigt. Für den geschlossenen Übergang der D_2 Linie finden wir theoretisch, dass das *nah-resonante Phasenkontrastverfahren* ein besseres Signal-zu-Rausch-Verhältnis als das Absorptionsverfahren liefert. Wir berichten über die Entwurf und den Aufbau des Phasenkontrastsystems. Um die genaue Atomzahl in einer mesoskopischen Wolke zu bestimmen, wurde eine Kalibrierung des Phasenkontrastsystems durchgeführt und diskutiert. Eine erste Abschätzung der Empfindlichkeit des Phasenkontrastsystem deutet darauf hin, dass dieses auch für dünne Wolken mit dem Absorptionsverfahren konkurrieren kann.

Phase contrast imaging of mesoscopic Bose-Einstein condensates

We theoretically and experimentally investigate the performance of phase contrast imaging for the observation of mesoscopic Bose-Einstein condensates of ^{87}Rb. We especially consider a new regime of phase contrast imaging by tuning the saturated probe beam only a few linewidths away from resonance. Theoretically, *near-resonant phase contrast imaging* is found to deliver a better signal-to-noise ratio than saturation absorption imaging for the cycling transition of the D_2 line. We then report on the design and implementation of a phase contrast system. Finally, the latest achievements concerning the calibration of this phase contrast system in order to precisely deduce the number of atoms in a mesoscopic BEC is presented and discussed. A first estimation of the atom number sensitivity given by near-resonant phase contrast imaging suggests performance competitive with absorption imaging.

Contents

1 Introduction

The best technique to probe cold atoms in a vacuum chamber depends strongly on the particular experiment to be performed, the type of atoms, the trapping method, the density etc. Certainly, a good way to probe cold atoms has to be an optical imaging technique since the only information about atoms that comes out of a vacuum chamber takes the form of light.

Shining light on atoms gives rise to three main phenomena: first, atoms can absorb a fraction of the light, second, they can re-emit the absorbed light in an other arbitrary direction. In this way, atoms become visible because they first produce a shadow and then act as secondary light sources. Absorption imaging corresponds to the interaction of the first kind, i.e. the recording of the light shadow. Fluorescence imaging, on the other hand, involves the recording of the re-emitted light, called fluorescence. The third atom-light interaction phenomenon arises even if the atoms are transparent. In this case, atoms still act on light by introducing a phase shift to the optical wave. Dispersive techniques such as phase contrast imaging rely on this special interaction.

Fluorescence imaging is the most sensitive imaging technique, mainly because it is background-free. Absorption imaging is less sensitive than fluorescence imaging because of the noise carried by the probe beam, which forms the background of the image. Still, absorption imaging recently succeeded in observing a single trapped ion (Streed et al. [1]). Phase contrast imaging is not reputed for its sensitivity but has clear advantages as a non-destructive imaging technique.

Our group commonly performs absorption imaging for the observation of meso-scopic Bose-Einstein condensates (BEC). The sensitivity of the technique is a crucial parameter for the study of quantum dynamics. For example, the observation of interferometric precision below the classical limit strongly relies on the sensitivity of the atom counting technique (Gross et al. [2]). Furthermore, improving the sensitivity to the single-atom level enables the observation of new phenomena such as odd-even effects. In this context, our group would like to achieve better atom resolution. Fluorescence imaging is a good candidate to reach the desired sensitivity and we recently demonstrated single atom sensitivity for clouds containing hundreds of atoms with fluorescence imaging. However, the implementation of fluorescence imaging to the existing BEC experiment is complicated for practical reasons. An alternative route, which has the advantage of being more easily implementable to the existing setup, is phase contrast imaging.

The aim of this thesis is to investigate the possible advantages of phase contrast imaging over absorption imaging in the observation of ultra cold atomic clouds.

In the first chapter, we begin with a self-consistent presentation of the theory of

imaging. Fourier optics is developed and applied to absorption and phase contrast imaging. In the second chapter, we compare both imaging techniques on a theoretical basis. For this purpose, we introduce an innovative way to perform phase contrast imaging. In contrast to other implementations, phase contrast is performed near-resonant and then becomes a destructive technique. In the last chapter, we report on the implementation of this technique in the existing BEC setup.

2 Theory of imaging

2.1 Fourier Optics

In the field of atomic physics, a satisfying treatment of the interaction of light and matter often requires at least a semiclassical theory with a quantized atom and a classical field. In instrumental optics however, a scalar wave theory is sufficient because we are mostly interested in the propagation of light through simple isotrope and transparent media. In this section, we present a sophisticated development of the scalar wave theory: **Fourier optics**. This theory will greatly facilitate the description of optical systems and especially the **phase contrast** method which is nothing but a spatial filtering. Fourier optics describes the propagation of waves in optical systems by means of simple successive Fourier transform and convolution operations. Numerical simulations of optical systems will then be greatly facilitate because Fourier transform and convolutions are easier to numerically implement than the Huygens-Fresnel principle for example.

Fourier optics is not an independent, well defined branch of optics with its own postulate and theorem. Instead, Fourier analysis appears naturally in instrumental optics and its association with linear system theory becomes a powerful tool to investigate optical systems.

We first begin with a short recall of the postulates and definition of wave optics. We then introduce the main results of the Fourier analysis and the linear system theory. Finally we exploit this knowledge to formulate the most important results of Fourier optics: a description of the propagation of light in free space, diffraction theory and the emergence of the Fourier transform in instrumental optics.

Because, in practice, we deal exclusively with coherent sources as lasers, we restrict our treatment to temporally and spatially correlated waves. This special treatment is often called **coherent imaging**.

This condensed presentation of Fourier optics strongly relies on the impressive books by Saleh and Teich [3] and Goodman [4] where illuminating illustrations and details can be found.

2.1.1 Reminder : Wave optics and Fourier analysis

Wave optics

Wave optics is the theory that describes light as being the manifestation of the propagation of waves. Waves are real functions $u(\mathbf{r}, t)$ of space and time that satisfies

the **wave equation**,

$$\nabla^2 u - \frac{1}{c^2}\frac{\partial^2 u}{\partial t^2} = 0, \tag{2.1}$$

with $\nabla^2 = \frac{\partial^2}{\partial x^2} + \frac{\partial^2}{\partial y^2} + \frac{\partial^2}{\partial z^2}$ and c the speed of light in the medium. Wave optics is then a **scalar** theory of light as opposed to the more general theory of electromagnetic optics where waves are **vectors**.

For visible light, our instruments (the eye or a photodiode for example) are not directly sensitive to the wavefunction $u(\mathbf{r}, t)$ but rather to the amount of energy carried by the waves. The wavefunctions defined above turn out to be the underlying quantity responsible for our energetic sensitivity to light

$$I(\mathbf{r}, t) = 2\left\langle u^2(\mathbf{r}, t)\right\rangle, \tag{2.2}$$

where I is the intensity in units of Joule per second per square meter in SI units and $\langle\,\rangle$ denotes a time average. Equations (2.1) and (2.2) are the main postulates of wave optics and carry an important knowledge about light: *the relevant quantity for describing light is not the measurable intensity but a rather more sophisticated quantity, the wavefunction.*

It is convenient (as will be seen with the Fourier analysis) to formulate wave optics by means of **complex** scalar wavefunctions $U(\mathbf{r}, t)$ so that $u(\mathbf{r}, t)$ is its real part and that also satisfies the wave equation

$$\nabla^2 U(\mathbf{r}, t) - \frac{1}{c^2}\frac{\partial^2 U(\mathbf{r}, t)}{\partial t^2} = 0. \tag{2.3}$$

An important solution of (2.3) is the complex wavefunction, which describes a **monochromatic wave**

$$U(\mathbf{r}, t) = U(\mathbf{r})\mathrm{e}^{-2\mathrm{i}\pi\nu t}, \tag{2.4}$$

where $U(\mathbf{r}) = A(\mathbf{r})\mathrm{e}^{\mathrm{i}\phi(\mathbf{r})}$ is called the **complex amplitude**, $A(\mathbf{r}) \in \mathbb{C}$ and $\phi(\mathbf{r}) \in \mathbb{R}$ are the amplitude and phase of the wave.

From the previous considerations, it can be shown that postulate (2.1) reduces, in the case of monochromatic waves, to the **Helmholtz equation**

$$\nabla^2 U + k^2 U = 0, \tag{2.5}$$

where $k = \frac{2\pi\nu}{c}$ is the wavenumber. Postulate (2.2) reduces to

$$I(\mathbf{r}) = |U(\mathbf{r})|^2. \tag{2.6}$$

Up to now and for the rest of this chapter, the monochromatic wave optics that follow from (2.5) and (2.6) is the underlying theory, so that we will always suppose the monochromaticity of waves. The simplest (monochromatic) wave of this theory is the plane wave $U(\mathbf{r}) = A\mathrm{e}^{\mathrm{i}\mathbf{k}\cdot\mathbf{r}}$, where $A \in \mathbb{C}$ and $\mathbf{k}$ is the wave vector pointing in the propagation direction with absolute value $k = \frac{2\pi}{\lambda}$. The plane wave is of great importance for two reasons:

- It is a useful idealized first approximation for most of the beams we are manipulating in the laboratory (collimated beams, Gaussian beams near the waist, waves out of a point like source at great distance), and its propagation through optical systems is straightforward.

- It is the physical counterpart of the harmonic functions of the Fourier analysis that we are going to introduce in the next section.

Fourier analysis

If $f : \mathbb{R}^2 \to \mathbb{C}$ is a piecewise smooth function and $\iint_{-\infty}^{\infty} |f(x,y)|\ \mathrm{d}x\ \mathrm{d}y$ exists, i.e. if $f(x,y)$ is integrable, then f can be written as the weighted superposition integral of harmonic functions

$$f(x,y) = \iint_{-\infty}^{+\infty} \underbrace{W(f_x, f_y)}_{\text{weight}}\ \underbrace{e^{2\mathrm{i}\pi(xf_x+yf_y)}}_{\text{harmonic functions}}\ \mathrm{d}f_x\ \mathrm{d}f_y. \tag{2.7}$$

The continuous weight function $W(f_x, f_y)$ is called the **Fourier transform** of f and reads

$$W(f_x, f_y) = \iint_{-\infty}^{+\infty} f(x,y)\ e^{-2\mathrm{i}\pi(f_x x+f_y y)}\ \mathrm{d}x\ \mathrm{d}y. \tag{2.8}$$

We will use the notation $\mathcal{F}[f](f_x, f_y)$ or simply $\mathcal{F}[f]$ to denote the Fourier transform of f. $\mathcal{F}[f]$ is itself a complex function with the same amount of information as in f. Equation (2.7) shows that it is possible to transform $\mathcal{F}[f]$ back into its original form f. Thus, we define the **inverse Fourier transform** of a function $W(f_x, f_y)$:

$$\mathcal{F}^{-1}[W](x,y) = \iint_{-\infty}^{+\infty} W(f_x, f_y)\ e^{2\mathrm{i}\pi(xf_x+yf_y)}\ \mathrm{d}f_x\ \mathrm{d}f_y. \tag{2.9}$$

We will assume that physical functions (complex amplitude in a plane) that we are going to Fourier transform always satisfy the existence conditions, namely that functions are smooth and integrable.

Nevertheless, in the course of our discussion it will be convenient to deal with functions that do not satisfy the existence conditions but still have a Fourier transform. Two examples are the Dirac delta[1] $\delta(x - x_0, y - y_0)$ and $\exp(\mathrm{i}\,2\pi(\nu_x x + \nu_y y))$

---

[1]We define the delta function by the equations

$$\begin{cases} \delta(x - x_0) = 0, \ \text{when } x \neq x_0, \\ \int_{-\infty}^{+\infty} \delta(x - x_0)\mathrm{d}x = 1. \end{cases}$$

We will make use of the property

$$\int_{-\infty}^{+\infty} \delta(x - x_0)f(x)\mathrm{d}x = f(x_0).$$

with $\nu_x, \nu_y \in \mathbb{R}$. Using the property of the Dirac function given in the footnote of page 14 as well as the definition of the Fourier transform, one finds

$$\mathcal{F}[\delta(x - x_0, y - y_0)] = e^{-2i\pi(f_x x_0 + f_y y_0)}, \tag{2.10}$$

$$\mathcal{F}[\exp(i2\pi(\nu_x x + \nu_y y))] = \delta(f_x - \nu_x, f_y - \nu_y). \tag{2.11}$$

Another remarkable property of the Dirac delta is that it acts as unity under the **convolution product** operation. The convolution product is an operation on two functions $f(x, y)$ and $g(x, y)$ that produce a third function written $(f * g)(\xi, \eta)$ or simply $f * g$ using the following integral transform

$$(f * g)(\xi, \eta) = \iint_{-\infty}^{+\infty} f(x, y) \ g(\xi - x, \eta - y) \mathrm{d}x \ \mathrm{d}y. \tag{2.12}$$

The convolution is commutative, associative, distributive[2] and, as mentioned above, has the Dirac delta as identity:

$$f * \delta = f. \tag{2.13}$$

The name and properties of the convolution product suggests some resemblance with the usual scalar multiplication. The **convolution theorem** links the convolution product and the scalar multiplication using Fourier transforms

$$\mathcal{F}[f * g] = \mathcal{F}[f] \cdot \mathcal{F}[g], \tag{2.14}$$

and

$$\mathcal{F}[f \cdot g] = \mathcal{F}[f] * \mathcal{F}[g]. \tag{2.15}$$

2.1.2 Linear invariant system theory

We call a system a physical device that performs a mapping of a set of input phenomena into a set of output phenomena. The mathematical representation of the system is an operator S that for each input function $f(x, y)$ associates an output function $g(x, y)$,

$$g(x, y) = S[f(x, y)]. \tag{2.16}$$

---
[2]

        Commutativity: $f * g = g * f$,
        Associativity: $(f * g) * h = f * (g*)$,
        Distributivity: $f * (g + h) = f * g + f * h$.

Let us now rewrite the input function using (2.13) as a weighted superposition integral of δ functions,

$$f(x,y) = f * \delta = \iint_{-\infty}^{+\infty} f(x',y')\, \delta(x-x', y-y')\, \mathrm{d}x'\, \mathrm{d}y'. \tag{2.17}$$

Substitution of (2.17) into (2.16) gives

$$g(x,y) = S\left[\iint_{-\infty}^{+\infty} f(x',y')\, \delta(x-x', y-y')\, \mathrm{d}x'\, \mathrm{d}y'\right]. \tag{2.18}$$

If S is a linear operator [3], the system is called **linear** and relation (2.18) becomes

$$g(x,y) = \iint_{-\infty}^{+\infty} f(x',y')\, S[\delta(x-x', y-y')]\, \mathrm{d}x'\, \mathrm{d}y'. \tag{2.19}$$

From the definition of the operator S and the physical interpretation of the Dirac δ, $S[\delta(x-x', y-y')]$ is the response of the system to an input impulse phenomenon (point light source in optics) located at (x', y') in the input plane. It is therefore called **Impulse Response** or **point spread function (PSF)** in optics.

The PSF of a system is generally a function of the image plane variables (x, y) and two object plane parameters (x', y'). However, it is often possible to find a regime (a spatial region in optics) where the shape of the PSF is not sensitive to the absolute position of the input impulse phenomenon in (x', y'). In this region, $\mathrm{PSF}(x, y; x', y')$ is just a shifted version of $\mathrm{PSF}(x, y; 0, 0) = \mathrm{PSF}(x, y)$ and can be expressed as a function of two variables [4],

$$\mathrm{PSF}(x, y; x', y') = \mathrm{PSF}(x-x', y-y'). \tag{2.20}$$

A system is then called **invariant** and in this case (2.19) reduces to

$$g(x,y) = \iint_{-\infty}^{+\infty} f(x',y')\, \mathrm{PSF}(x-x', y-y')\, \mathrm{d}x'\, \mathrm{d}y'. \tag{2.21}$$

For linear invariant systems, the input-output relation is a convolution product,

$$f = g * \mathrm{PSF}. \tag{2.22}$$

The interpretation of the convolution relation is the following: The output signal is a blurred replica of the input where the blurring results from the spatial extent

---

[3]

        Linearity: $S[af_1 + bf_2] = aS[f_1] + bS[f_2]$.

[4] In order for the operation $x_o - x$ and $y_0 - y$ to make sense, x and y should be scaled-normalized compared to x_0 and y_0. For an optical system with magnification M, it would require the transformation $x, y \to Mx, My$ (See chapter 9.5 of Born and Wolf [5]).

of the PSF. In the limit of infinitely narrow PSF, PSF $= \delta$, the output is a perfect replica of the input.

Applying the convolution theorem (2.14) to the above convolution (2.22) leads to the relation:

$$\mathcal{F}[g] = \mathcal{F}[f] \cdot \mathcal{F}[\text{PSF}] \tag{2.23}$$

and

$$g = \mathcal{F}^{-1}[\mathcal{F}[f] \cdot \mathcal{F}[\text{PSF}]]. \tag{2.24}$$

The Fourier transform of the PSF, $\mathcal{F}[\text{PSF}](f_x, f_y)$, is called the **transfer function** of the system and is denoted by **TF**. The interpretation of the relation (2.23) is the following: The frequency spectrum of the output is a low-pass filtered version of the input spectrum. The transfer function states how well the input frequencies are transmitted in the system.

The general theory of linear invariant systems that we just introduced is well suited to describe optical systems if one considers the input and output function as being the complex amplitude in the object and image plane respectively. The linearity of such an optical system follows from the linearity of the Helmholtz equation. As mentioned earlier, for an optical system to be invariant (described by a 2D PSF), the shape of the PSF should be independent of the absolute location of the point source. For real optical systems, this can only be true within a region where aberrations are well corrected, because aberrations are position-dependent and tends to distort the PSF. *A linear invariant optical system needs to be diffraction limited.*

In the last section, we introduced the most important mathematical and physical tools to describe optical systems: complex amplitude, Fourier transform, the convolution product and the convolution theorem. We showed that a diffraction limited optical system can be equivalently characterized by its PSF or transfer function. *In the space domain, the image is a convolution of the object with the PSF. In the frequency domain, the image (spectrum) is a product of the object (spectrum) with the transfer function.* The Fourier transform enables to go from one domain to another without loss of information. In the next section, we are going to see that the Fourier transform emerges in different, independent manner giving its name to this branch of optics.

2.1.3 Fourier optics main results

In most cases, the complex amplitude underlying light phenomena is not known for every point in space. Rather than that, one has a partial knowledge of this complex amplitude, for example the complex amplitude can be known within a cavity, in a plane directly after a diaphragm or at the output of a laser. From this partial information, the propagation law of waves enables one to infer the complex amplitude in every other point in space. The propagation of previously spatially confined waves is usually called **diffraction**. In this section, we are going to summarize some

important results of diffraction theory, using Fourier analysis and optical system theory [5].

Spectral analysis of the complex Amplitude

Consider a plane wave $U(x, y, z) = A\mathrm{e}^{\mathrm{i}(k_x x + k_y y + k_z z)}$. If the wavelength λ is also known (which is the case in practice), the wave is over determined and actually, it is sufficient to know the complex amplitude in an arbitrary plane, say orthogonal to z. For example, in $z = 0$, the complex amplitude $U(x, y, 0) = U(x, y) = A\mathrm{e}^{\mathrm{i}(k_x x + k_y y)}$ fully determines the wave (A and $\mathbf{k}$ are known) since k_z can be deduced via the relation

$$\left(\frac{2\pi}{\lambda}\right)^2 = k_x^2 + k_y^2 + k_z^2.$$

It is therefore equivalent to describe a plane wave by the full 3D complex amplitude or just by a 2D harmonic function $U(x, y) = A\mathrm{e}^{\mathrm{i}2\pi(f_x x + f_y y)}$ *plus the wavelength, where* $f_{x,y} = \frac{k_{x,y}}{2\pi}$. If we now consider an arbitrary monochromatic wave (not necessarily a plane wave) with complex amplitude $U(x, y) = A(x, y)\mathrm{e}^{\mathrm{i}\varphi(x,y)}$ in the plane defined by $z = 0$, this wave can be Fourier analysed in an integral superposition of harmonic functions

$$U(x, y) = \iint_{-\infty}^{+\infty} \mathcal{F}[U](f_x, f_y) \underbrace{\mathrm{e}^{\mathrm{i}2\pi(x f_x + y f_y)}}_{\text{harmonic functions}} \ \mathrm{d}f_x \ \mathrm{d}f_y. \tag{2.25}$$

To each harmonic function corresponds a plane wave $\mathrm{e}^{\mathrm{i}2\pi(x f_x + y f_y)}\mathrm{e}^{\mathrm{i}k_z z}$ so that the overall wave can be written as follows

$$U(x, y, z) = \iint_{-\infty}^{+\infty} \mathcal{F}[U](f_x, f_y) \underbrace{\mathrm{e}^{\mathrm{i}2\pi(x f_x + y f_y)}\mathrm{e}^{\mathrm{i}k_z z}}_{\text{Plane wave}} \ \mathrm{d}f_x \ \mathrm{d}f_y, \tag{2.26}$$

where $k_z = 2\pi\sqrt{\lambda^{-2} - f_x - f_y}$. *An arbitrary wave can then be seen as the superposition of plane waves*[6].

Free space propagation

The plane wave superposition relation (2.26) can be used to describe the free space propagation. Indeed, if $U(x, y, 0)$ is known, the complex amplitude in every other plane z can be determined. Let us consider the propagation of the wave from the

---

[5]The most popular way to build the scalar diffraction theory is to start from the **Huygens-Fresnel principle** as depicted for example in Goodman [4]. We present here an alternative way following Saleh and Teich [3], where Fourier analysis is of much importance.

[6]The complex amplitude $\mathrm{e}^{\mathrm{i}2\pi(x f_x + y f_y)}\mathrm{e}^{\mathrm{i}k_z z}$ with $k_z = 2\pi\sqrt{\lambda^{-2} - f_x - f_y}$ describes a propagating plane wave only if $k_z \in \mathbb{R}$. If $\lambda^{-2} - f_x - f_y < 0$, k_z becomes imaginary and the wave turns out to be evanescent.

plane $z = 0$ with complex amplitude $f(x, y) = U(x, y, 0)$ to the plane $z = d$ with complex amplitude $g(x, y) = U(x, y, d)$, (2.26) becomes

$$g(x, y) = \iint_{-\infty}^{+\infty} \mathcal{F}[f(x, y)] \, \text{TF}_{\text{fs}} \, \mathrm{e}^{\mathrm{i}2\pi(xf_x + yf_y)} \, \mathrm{d}f_x \, \mathrm{d}f_y, \tag{2.27}$$

where $\text{TF}_{\text{fs}} = \mathrm{e}^{\mathrm{i}2\pi d \sqrt{\lambda^{-2} - f_x - f_y}}$. Relation (2.27) is the inverse Fourier transform of the product of two function, $\mathcal{F}[f]$ and TF_{fs}. Identifying (2.27) with (2.24), TF_{fs} appears to be the transfer function of a system with input $f(x, y)$ and output $g(x, y)$,

$$\text{TF}_{\text{fs}}(f_x, f_y) = \mathrm{e}^{\mathrm{i}2\pi d \sqrt{\lambda^{-2} - f_x - f_y}}. \tag{2.28}$$

This system is the most simple one: It is a **free space** interval of length d. The integral (2.27) is not analytically solvable, and historically an approximation for small spatial frequencies compared to λ^{-1} is of great importance because it leads to analytical results[7]. This is the **Fresnel approximation** and the transfer function of free space reduces to

$$\text{TF}_{Fresnel} = \mathrm{e}^{\mathrm{i}kd}\mathrm{e}^{-\mathrm{i}\pi\lambda d(f_x^2 + f_y^2)}, \tag{2.29}$$

with $k = \frac{2\pi}{\lambda}$. The PSF of free space is the inverse Fourier transform of the transfer function

$$\text{PSF}_{Fresnel}(x, y) = \mathcal{F}^{-1}[\text{TF}_{Fresnel}] = -\frac{\mathrm{i}}{\lambda d} \, \mathrm{e}^{\mathrm{i}kd} \, \mathrm{e}^{\mathrm{i}k\frac{x^2 + y^2}{2d}}. \tag{2.30}$$

Gaussian beam

The Gaussian beam is a wave (solution of Helmholtz equation) of great interest because it can nicely approximate beams coming out of a single mode fibre or laser for example. Theoretically speaking, it is a non-trivial solution of the Helmholtz equation,

$$U(x, y, z) = \frac{A}{1 + \mathrm{i}z/z_R} \, \exp\left[-\frac{x^2 + y^2}{w_0^2(1 + z^2/z_R^2)}\right] \exp\left[\mathrm{i}k\left(z + \frac{x^2 + y^2}{2(z + z_r^2/z)}\right)\right] \tag{2.31}$$

where $z_r \in \mathbb{R}$ is the Rayleigh range and w_0 the waist of the beam.

We now briefly argue why this particular wave arises in the context of single mode lasers and fibres:

- In a laser cavity, the boundary conditions imposed by the spherical mirrors constrain the wave to be a Hermite-Gaussian beam (see Chapter 3.3 of Saleh and Teich [3]) because Hermite-Gaussian beams can exist self-consistently within a pair of spherical mirrors. Finally, the circular and finite aperture of the mirrors favours the Gaussian beam among the other beams because it has the smallest radial extension and hence minimize the resonator losses (see Chapter 10.2 of Saleh and Teich [3]).

---

[7]In the Taylor expansion of the square root $\sqrt{1 - \lambda^2 f_x^2 - \lambda^2 f_y^2} = 1 - \frac{\lambda^2 f_x^2 - \lambda^2 f_y^2}{2} + ...$, just the quadratic terms are taken into account.

- The reason for the light coming out of a single mode fibre being almost a Gaussian beam is different and related to Fourier optics. The mode propagating in a single mode fibre has a bell radial distribution similar to a Gaussian profile (see Chapter 9.2 of Saleh and Teich [3]). Furthermore, it can be shown that the wave propagating out of an aperture with Gaussian amplitude profile is exactly the Gaussian beam (2.31). Since the complex amplitude profile at the output of a single mode fibre is nearly Gaussian, the outgoing beam is also nearly Gaussian.

We now summarize the principal properties of the Gaussian beam:

- The intensity profile $I = |U|^2$ is a Gaussian function in the transversal plane $z = d$,

$$I(x, y, d) = \frac{I_0}{1 + \left(\frac{d}{z_r}\right)^2} \exp\left[-\frac{2(x^2 + y^2)}{w(d)^2}\right], \qquad (2.32)$$

where $w(d) = w_0\sqrt{1 + \left(\frac{d}{z_r}\right)^2}$ is the beam width at coordinate $z = d$ and $I_0 = |A|^2$ is the peak intensity.

- The beam width is the distance from the optical axis where intensity decreased by a factor $1/e^2$ and the amplitude by a factor $1/e$. The beam width at the origin is the waist w_0.

- Two parameters suffice to fully determined a Gaussian beam. For example, the waist w_0 and the wavelength λ gives the divergence angle $2\theta_0 = \frac{2\lambda}{\pi w_0}$ and the depth of focus $2z_r = \frac{2\pi w_0^2}{\lambda}$.

- Focusing a Gaussian beam (w_0, z_r) with a lens gives rise to another Gaussian beam with different waist w_0'. In the case where the depth of focus z_r is much longer than the focal length of the lens f, the new waist of the focused beam is

$$w_0' = \frac{\lambda f}{\pi w_0}, \qquad (2.33)$$

located at a distance f from the lens (in the geometrical focus).

Fraunhofer diffraction

The Fresnel diffraction theory that follows from equations (2.29) or (2.30) is valid when the input amplitude $f(x, y)$ contains only *small* spatial frequencies. The amplitude in the output plane $g(x, y)$ is the convolution product

$$g(x, y) = f(x, y) * \text{PSF}_{Fresnel}(x, y)$$
$$\propto \iint_{-\infty}^{+\infty} f(x', y')\, e^{i\pi \frac{x'^2 + y'^2}{\lambda d}} e^{-2i\pi\left(\frac{x}{\lambda d}x' + \frac{y}{\lambda d}y'\right)}\, dx'\, dy', \qquad (2.34)$$

which is the Fourier transform of $f(x, y)\,\mathrm{e}^{\mathrm{i}\pi\frac{x'^2+y'^2}{\lambda d}}$, the input amplitude multiplied by a quadratic phase factor. If we assume further that the input amplitude is non-zero only within a small area compared to the free-space distance d, the phase factor $\mathrm{e}^{\mathrm{i}\pi\frac{x'^2+y'^2}{\lambda d}}$ contributes to the integral only for small (x', y'), where it almost equals unity: $\mathrm{e}^{\mathrm{i}\pi\frac{x'^2+y'^2}{\lambda d}} \approx 1$. This approximation leads to a simple Fourier transform relation between the output and input amplitudes[8],

$$
\begin{aligned}
g(x, y) &= f(x, y) * \mathrm{PSF}_{Fresnel}(x, y), \\
&\propto \iint_{-\infty}^{+\infty} U(x', y', 0)\,\mathrm{e}^{-2\mathrm{i}\pi(\frac{x}{\lambda d}x' + \frac{y}{\lambda d}y')}\,\mathrm{d}x'\,\mathrm{d}y', \\
&\propto \mathcal{F}[f(x, y)]\left(\frac{x}{\lambda d}, \frac{y}{\lambda d}\right),
\end{aligned}
\tag{2.35}
$$

where d is the distance between the input plane and the output plane. The complex proportionality factor is $-\frac{\mathrm{i}}{\lambda d}\,\mathrm{e}^{\mathrm{i}kd}\,\mathrm{e}^{\mathrm{i}k\frac{x^2+y^2}{2d}}$. This approximation is called the Fraunhofer approximation or the **far field** approximation. Typical observation distances of the Fraunhofer diffraction pattern originating from a circular aperture of diameter $1\,\mathrm{mm}$ are at least a few meters.

Fourier transform property of a converging system

We can understand qualitatively the emergence of the optical Fourier transform in the following way: we defined the Fourier transform of a function $f(x, y)$ as the continuous weight of the harmonic functions (plane waves) that, once superimposed, equal the function $f(x, y)$ (as defined in Equation 2.7). Performing an optical Fourier transformation is nothing but having access to the amplitude of each plane waves that composes the input function.

A practical method to separate the plane waves and record their amplitudes is to use a converging optical system. In the back focal plane of a diffraction limited converging system, the different plane waves focus onto a point (x,y) with coordinates proportional to the plane wave associated spatial frequency ($x \propto f_x$, $y \propto f_y$).

Following this reasoning leads to the Fourier transform property of a converging system: The amplitude in the front ($f(x, y)$) and back focal plane ($g(x, y)$) of a converging system forms a Fourier transform pair,

$$
\begin{aligned}
g(x, y) &= \frac{-i}{\lambda f}\,\mathrm{e}^{2\mathrm{i}kf}\,\iint_{-\infty}^{+\infty} f(x', y')\,\mathrm{e}^{-2\mathrm{i}\pi(\frac{x}{\lambda f}x' + \frac{y}{\lambda f}y')}\,\mathrm{d}x'\,\mathrm{d}y', \\
&= \frac{-i}{\lambda f}\,\mathrm{e}^{2\mathrm{i}kf}\,\mathcal{F}[f]\left(\frac{x}{\lambda f}, \frac{y}{\lambda f}\right),
\end{aligned}
\tag{2.36}
$$

where f is the focal length of the diffraction limited converging system.

---

[8]The conditions of validity of the Fraunhofer approximation can be found in Saleh and Teich [3].

PSF of an optical system

In the last sections, we showed that the imaging of a diffraction limited system can be fully described by its point spread function. We now aim to discuss how to efficiently determine this function knowing the optical system properties.

One way to do this would be to calculate how a (spherical) wave emitted by a single point source in the object plane propagates through the system and ends up in the image plane. This method is correct but would require a lot of calculations, especially if the system has multiple optical elements.

The computation of the PSF is considerably simplified by a theorem that relates the PSF of an optical system with the Fourier transform of the **exit pupil**[9] function,

$$
\begin{aligned}
PSF(x, y) &= \frac{1}{\lambda^2 d^2} \iint_{-\infty}^{+\infty} P(x', y')\, \mathrm{e}^{-2\mathrm{i}\pi(xx' + yy')} \, \mathrm{d}x' \, \mathrm{d}y', \\
&= \frac{1}{\lambda^2 d^2} \, \mathcal{F}\left[P\right](x, y),
\end{aligned}
\tag{2.37}
$$

where P is the exit pupil function, defined as unity inside the exit pupil and zero otherwise. d is the distance between the exit pupil and the image plane.

2.2 Imaging dense clouds of atoms

2.2.1 The light - atomic cloud interaction

The atomic cloud model

The experimental atomic transition of interest is a 5s-5p dipole transition in the alkali atom, ^{87}Rb. For a **two-level atom** interacting with a near resonant electromagnetic field, the semiclassical theory predicts a charge density oscillation at the generalized Rabi frequency (see chapter 3 of Meystre and III [6]). This **quantum mechanical** result shares some analogy with the **Lorentz oscillator model** [10] where a harmonically bound charge (the outer electron of ^{87}Rb) oscillates at the optical radiation frequency around the positive core. This motivates the model of the atomic cloud as a dielectric, **linear** and **dispersive** medium so that the (complex amplitude) dipole moment p of one atom is proportional to the (complex amplitude) electric field E,

$$
p(\nu) = \alpha(\nu)E
\tag{2.38}
$$

where $\alpha(\nu)$ is the frequency dependent complex polarisability. As will be shown in the next sections, the complex polarisability enables the treatment of both dispersion

---

[9]The exit pupil is the image, seen from the image space, of the most limiting aperture of the optical system. For more details, see Born and Wolf [5]. In the case of a two lens imaging system, the limiting aperture is the smallest lens.

[10]See Saleh and Teich [3] and Grimm et al. [7].

and absorption of the cloud. A more general treatment that takes into account the ground and excited state manifold, the anisotropy of the atom as well as the light polarisation can be found in Meppelink et al. [8].

The complex polarisability

Equation (2.38) is our definition of the complex polarisability. We will now make use of the Lorentz oscillator model in order to derive the polarisability of an atom in the cloud. The equation of motion of a driven, damped harmonic oscillator describing the motion of the bound external electron in the radiation field is

$$\ddot{x} + \sigma \dot{x} + w_0 x^2 = -\frac{e\mathbf{E}(t)}{m_e}, \tag{2.39}$$

where σ is the damping rate (in units of s^{-1}) due to radiation energy loss, w_0 the optical resonance angular frequency, $-e$ and m_e are the charge and mass of the electron and $\mathbf{E}(t)$ is the real electric field. The damping rate (defined as the prefactor of the $\dot{x}$ term) can be evaluated from Larmor's formula (see chapter 14 of Jackson [9]) for the power radiated by an accelerated charge,

$$\mathrm{P} = \frac{e^2 \ddot{x}^2}{6\pi\epsilon_0 c^3}, \tag{2.40}$$

where ϵ_0 is the vacuum permittivity and c is the speed of light. Assuming that the damping is much smaller than the optical frequency, the Abraham-Lorentz force $\mathbf{F}_{\mathrm{rad}}$ (also called radiative reaction force. See chapter 17 of Jackson [9]) reduces to a frictional force,

$$\mathbf{F}_{\mathrm{rad}} = \frac{e^2 w^2 \dot{x}}{6\pi\epsilon_0 c^3}, \tag{2.41}$$

where w is the electric field angular frequency. The damping rate of the equation of motion finally reads,

$$\sigma = \frac{e^2 w^2}{6\pi\epsilon_0 m_e c^3}. \tag{2.42}$$

Multiplying both sides of the equation of motion (2.39) by $-e$ reveals an equation for the dipole moment,

$$\ddot{\mathbf{p}} + \sigma \dot{\mathbf{p}} + w_0 \mathbf{p}^2 = \frac{e^2 \mathbf{E}(t)}{m_e}. \tag{2.43}$$

Substitution of $\mathbf{E}(t) = \Re\{E \exp(-iwt)\}$ and $\mathbf{p}(t) = \Re\{p \exp(-iwt)\}$ into (2.43) leads to the wanted linear relation between p and E,

$$p = \frac{e^2}{m_e} \frac{1}{w_0^2 - w^2 - iw\sigma} E, \tag{2.44}$$

from which we identify the complex polarisability,

$$\alpha = \frac{e^2}{m_e} \frac{1}{w_0^2 - w^2 - iw\sigma},$$
$$= 6\pi\epsilon_0 c^3 \frac{\Gamma/w_0^2}{w_0^2 - w^2 - i(w^3/w_0^2)\Gamma}, \tag{2.45}$$

where we introduced the on-resonance damping rate $\Gamma = (w_0/w)^2\sigma$. In typical imaging conditions, the probe light detuning $|w - w_0|$ is much smaller than the resonance angular frequency w_0 so that the so-called *rotating wave approximation* is well justified and $w/w_0 \approx 1$ and $w_0^2 - w^2 = (w_0 + w)(w_0 - w) \approx 2w_0(w_0 - w)$. The expression of the polarisability becomes

$$\alpha = \frac{3}{(2\pi)^2}\epsilon_0\lambda^3 \frac{\Gamma}{2(w_0 - w) - i\Gamma}. \tag{2.46}$$

Index of refraction and absorption of an atomic cloud

In phase contrast imaging, we are mainly interested in the phase shift introduced by the cloud in contrast to absorption imaging where absorption is of much importance. It is possible to handle both phenomena with the unique complex polarisability. The real part of the polarisability is related to the index of refraction of the cloud and the imaginary part to the absorption, as can be seen in chapter 5 of Saleh and Teich [3].

In the case of a dilute media (such as a cold atomic cloud, thermal or BEC, in vacuum), the index of refraction n_{ref} and the absorption coefficient α_{Abs} (in the sense of the Beer-Lambert law) are given by

$$n_{ref} = 1 + \frac{n}{2\epsilon_0}\mathrm{Re}\{\alpha\} \quad \text{and}$$
$$\alpha_{Abs} = \frac{2\pi n}{\lambda\epsilon_0}\mathrm{Im}\{\alpha\}, \tag{2.47}$$

where n is the position-dependent cloud density. The real and imaginary part of the polarisability in the rotating wave approximation are

$$\mathrm{Re}\{\alpha\} = \frac{-3}{(2\pi)^2}\epsilon_0\lambda^3 \frac{\delta}{1 + \delta^2} \quad \text{and}$$
$$\mathrm{Im}\{\alpha\} = \frac{3}{(2\pi)^2}\epsilon_0\lambda^3 \frac{1}{1 + \delta^2}, \tag{2.48}$$

where $\delta = \frac{w - w_0}{\Gamma/2}$ is the detuning in half linewidths. Finally, the index of refraction and the absorption read

$$n_{ref} = 1 - \frac{n\sigma_0\lambda}{4\pi} \frac{\delta}{1 + \delta^2}$$
$$\alpha_{Abs} = n\sigma_0 \frac{1}{1 + \delta^2}, \tag{2.49}$$

where we introduced the resonant cross section $\sigma_0 = 3\lambda^2/(2\pi)$. It is now possible to determine the most important parameters for phase contrast and absorption imaging, namely the **phase shift** and the **transmission coefficient**.

Assuming probe light propagating in the z direction through an inhomogeneous cloud, the accumulated phase is given by

$$\phi(x,y) = \frac{2\pi}{\lambda} \int_{-\infty}^{+\infty} [n_{ref}(x,y,z) - 1] \, \mathrm{d}z. \tag{2.50}$$

Substitution of (2.47) into (2.50) leads to the phase shift of Ketterle et al. [10],

$$\phi(x,y) = -\frac{\sigma_0}{2} \frac{\delta}{1+\delta^2} n_c, \tag{2.51}$$

where we introduced the column density $n_c = \int_{-\infty}^{+\infty} n \mathrm{d}z$.

The transmission coefficient(defined as the ratio of amplitudes $\sqrt{I_f}/\sqrt{I_0}$ after and before the cloud) follows from the Beer-Lambert law

$$\mathrm{d}I = -\alpha_{abs} I \mathrm{d}z. \tag{2.52}$$

The square of the transmission coefficient is the ratio of intensities,

$$t^2 = \frac{I_f}{I_i} = \mathrm{e}^{-\int_{z_i}^{z_f} \alpha_{abs} \, \mathrm{d}z}. \tag{2.53}$$

Substitution of (2.47) into (2.53) leads to the transmission coefficient

$$t = \mathrm{e}^{-\frac{\sigma_0}{2} \frac{1}{1+\delta^2} n_c}. \tag{2.54}$$

The most critical approximations done up to now are the two-level approximation and the classical derivation of the damping rate that neglects saturations effects. The polarisability in the case of saturation of the dipole transition can be derived from the optical Bloch equations (see Chapter 2 of Loudon [11]) and reads for the cycling transition of ^{87}Rb,

$$\alpha = \frac{\sigma_0 \epsilon_0}{k} \frac{1}{1+\delta^2 + I/I_{sat}} \left[-\delta + i\right], \tag{2.55}$$

where I_{sat} is the saturation intensity and $k = 2\pi/\lambda$ the wave number.

Scattering rate

Some aspects of imaging such as the fluorescence or the radiative pressure are easier to handle within the *photon picture*. From this point of view, the opacity of an atomic cloud with respect to resonant light is due to **scattering** of probe photons by the atoms: the absorption of photons and their isotropic re-emission.

Furthermore, in the semi-classical theory, the damping rate Γ corresponds to the decay rate $1/\tau$, where τ is the lifetime of the excited state. The scattering rate Γ_{sc}
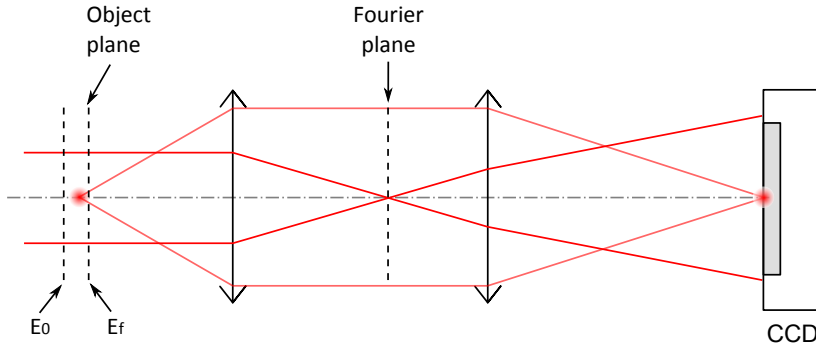
Figure 2.1: Absorption imaging setup with a two-lens optical system.

is then given by $\Gamma \rho_{ee}$, where ρ_{ee} is the *population* of the excited state. A steady state solution of the *optical Bloch equations* (see Steck [12]) yields the excited state population and therefore

$$\Gamma_{sc} = \frac{\Gamma}{2} \frac{I/I_{sat}}{1 + \delta^2 + I/I_{sat}}, \tag{2.56}$$

where I_{sat} is the saturation intensity, δ the detuning in half linewidths. Note that when the transition is saturated, the excited state population settles to $1/2$ and the scattering rate to $\Gamma/2$ which is around $18 \times 10^6 \, \text{s}^{-1}$ for the $5^2\text{S}_{1/2} \rightarrow 5^2\text{P}_{3/2}$ transition of ^{87}Rb (see Steck [12]).

2.2.2 Absorption imaging

When a collimated probe beam shines on an opaque object, it projects a shadow. **Absorption imaging** is nothing but the recording of this shadow. Because typical atomic clouds are small, and light is diffracted on them, the geometrical shadow vanishes within a few millimetres. Practically, it is not possible to place a photosensitive detector behind the atoms on the path of the probe beam. Rather than that, an imaging system images the shadow onto a CCD camera as seen in Figure 2.1.

In the last section, we related the transmission of light through the clouds to the column density so that an image represents a column density profile. As shown in Ketterle et al. [10], the maximum signal is obtained for **resonant probe light** ($\delta = 0$) so that the atoms introduce no phase shift at all (see Equation (2.51)). In this case, and in the low saturation limit, the transmission given by Equation (2.54) reduces to

$$t = \text{e}^{-\frac{\sigma_0}{2} n_c}. \tag{2.57}$$

By definition, the transmission coefficient is the ratio $t = E_f/E_0$ where E_0 and E_f are the amplitudes right before and right after the cloud, respectively. The amplitude right after the cloud is

$$E_f = t E_0, \tag{2.58}$$

where $t = t(x, y)$ is position-dependant. Assume an imaging system with unit magnification that images the amplitude E_f onto a CCD camera placed in the image plane. The camera records

$$
\begin{aligned}
I_f &= |E_f|^2 = |tE_0|^2, \\
&= t^2 I_0.
\end{aligned}
\tag{2.59}
$$

where I_0 is the position dependant probe light intensity[11]. Thus, the recorded intensity is a function of the cloud column density,

$$
I_f = I_0 e^{-\sigma_0 n_c},
\tag{2.60}
$$

and inversion of (2.60) results in

$$
n_c = -\frac{1}{\sigma_0} \ln\left(\frac{I_f}{I_0}\right),
\tag{2.61}
$$

where I_f and I_0 are the intensities measured with and without atoms, respectively.

A more general treatment taking into account a non-unity magnification as well as diffraction effects can be found in Appendix A. A general version of Equation (2.61), considering saturation, can be found in Reinaudi et al. [13] and will be discussed in the next chapter.

2.2.3 Phase contrast imaging

Phase contrast imaging is a slightly more subtle way to access to the column density profile. As seen before, the column density does not just appear in the transmission coefficient, but also into the phase shift (2.51). An alternative to absorption imaging is to record the phase shift instead of the shadow of the atoms. This implies two changes:

1. The probe light has to be **detuned from resonance** in order for the atoms to introduce a detectable phase shift.

2. The optical system has to be upgraded to a homodyne detection system.

Among homodyne techniques, phase contrast imaging has the advantage over interferometers to be less bulky and to be more easily adaptable to a standard imaging system.

In phase contrast imaging the reference radiation is the probe beam itself, phase shifted in order to interfere with the diffracted wave from the atoms.

As before, E_0 and E_f refer to the probe beam amplitude before and right after the atomic cloud; they are related by an amplitude and a phase factor[12]

$$
E_f = E_0 t e^{i\phi},
\tag{2.62}
$$

---

[11]We neglect here, for simplicity, the diffraction by the imaging system.

[12]Relation (2.62) as well as (2.58) are valid if the thickness of the cloud is small compared to the collimated probe beam diameter.

where ϕ is the phase shift caused by the atoms[13].

We now, in anticipation of what follows, make use of the liberty to write E_f as a superposition of two waves $E_f = E_0 + E_a$ where

$$E_a = E_0(te^{i\phi} - 1). \tag{2.64}$$

Because E_a is non-zero only in the presence of atom, we can consider E_a as the wave emitted by the atoms.

We choose these waves because they propagates in distinct ways through the imaging system. The collimated probe wave E_0 will be brought to focus in the back focal plane of the objective. In contrast, the diffracted wave E_a will not focus, but instead will be spread out on a large area in the back focal plane of the objective. This can be understood as a consequence of the Fourier transform property of the objective: E_0 is a low spatial frequency wave focusing in the focal point of the objective; E_a carries higher spatial frequencies and will then cross the back focal plane occupying a large area.

As recognised by Zernike [14], phase fluctuations (caused by the atomic cloud) will remain invisible as long the two waves E_0 and E_f present the same phase relation in the object and image plane. Indeed, the amplitude in the image plane, being an exact replica of the field in the object plane, the intensity measured in the image plane is the same as for absorption imaging,

$$
\begin{aligned}
\left| E_0 + E_0(te^{i\phi} - 1) \right|^2 &= \left| E_0 te^{i\phi} \right|^2, \\
&= t^2 I_0,
\end{aligned}
\tag{2.65}
$$

which presents no phase dependence.

Zernike idea is to phase shift the probe wave[14] by $-\frac{\pi}{2}$ compared to the atomic wave E_a. This is done by the mean of a particular **phase plate** shown in Figure 2.2. The resulting interferences between E_0 and E_a lead to an intensity pattern in the image plane that is dependent on the atomic phase shift.

In the presence of this phase plate, the amplitude in the image plane of a unitary magnifying optical system is

$$E_{CCD} = E_0 e^{-i\frac{\pi}{2}} + E_a. \tag{2.66}$$

---

[13]Note that the phase of Equation (2.62) is defined to within a constant φ,

$$E_f = E_0 te^{i(\phi + \varphi)}, \tag{2.63}$$

without practical consequences. However, for the simplicity of the following derivation, we require $\phi + \varphi$ to have zero mean and will continue to call this phase ϕ.

[14]A negative phase shift occurs with a phase plate that advances the phase of the unscattered wave E_0 compared to E_a.
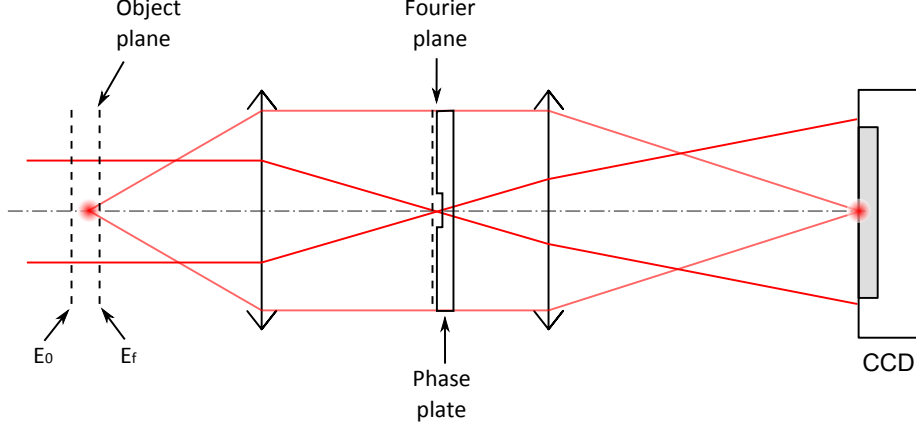
Figure 2.2: Phase contrast imaging setup with a two-lens optical system.

Substitution of (2.64) into (2.66) leads to the intensity seen by the camera,

$$
\begin{aligned}
I_{CCD} &= \left| -iE_0 + E_0(te^{i\phi} - 1) \right|^2, \\
&= |E_0|^2 \left| -i + te^{i\phi} - 1 \right|^2, \\
&= I_0 \left[2 + t^2 - 2t(\cos\phi + \sin\phi) \right].
\end{aligned}
\tag{2.67}
$$

If we assume small phase shifts from the atoms so that $\cos\phi \approx 1$ and $\sin\phi \approx \phi$, the intensity measured by the camera reduces to

$$
I_{CCD} = I_0(2 + t^2 - 2t - 2t\phi).
\tag{2.68}
$$

The phase shift is then a linear function of the normalised intensity difference,

$$
\phi = -\frac{1}{2t}\frac{I_{CCD} - I_0}{I_0} + \frac{(t-1)^2}{2t}.
\tag{2.69}
$$

If we now substitute (2.51) into (2.69), we find the column density to be

$$
n_c = \frac{1 + \delta^2}{t\sigma_0\delta} \left[\frac{I_{CCD} - I_0}{I_0} - (t-1)^2 \right],
\tag{2.70}
$$

where I_{CCD} is the intensity measured in the presence of atoms, I_0 the intensity measured without atoms, σ_0 is the resonant cross section and δ the detuning in half linewidths.

In appendix A, we generalise the treatment of phase contrast imaging considering the absorption of the phase plate and the magnification of the system. We also discuss the effect of the phase dip size.

3 Comparison of absorption and phase contrast imaging

Phase contrast imaging in the non-destructive regime (high detuning) has been applied with success and is well documented (see for example Meppelink et al. [8]). It offers clear advantages compared to absorption imaging in the observation of large Bose-Einstein condensates and for in-situ measurements (see Ketterle et al. [10]). For low optical densities ($n_c\sigma_0 < 1$), phase contrast presents no advantages.

In this chapter, we compare both techniques for the observation of clouds in ballistic expansion with moderate optical densities ($n_c\sigma_0 \approx 10$). This requires absorption imaging to be performed with highly saturated probe light and phase contrast to be performed near resonant.

3.1 Signal-to-noise comparison

Quantitative imaging requires the best possible signal sensitivity for a sufficient density dynamic range. Here we theoretically investigate the performance of absorption imaging and phase contrast imaging for the observation of small atomic clouds. The typical column density range of such clouds is between 0 and 40 atoms per square micrometer (or optical densities $n_c\sigma_0$ between 0 and 10). This is one order of magnitude more dilute than a condensed BEC but still two orders of magnitude denser than a cloud in a magneto-optical trap. For the sake of simplicity, we keep the light-atom interaction theory at a simple level neglecting polarisation effects and the multilevel structure of the atom. We assume the imaging transition to be the cycling transition of ^{87}Rb, so that we can use the polarisability (2.55). Phase contrast imaging is implicitly performed in the **positive** optimal regime where atoms appear brighter than the background ($-\pi/2$ phase plate and blue-detuned light).

3.1.1 Saturation absorption imaging

As described by Ketterle et al. [10], the best imaging sensitivity is obtained – in the low intensity regime – with absorption imaging. Phase contrast imaging has a factor 2 lower sensitivity in optimal conditions ($\pm\pi/2$ phase plate and at the detuning $\delta = 1$ in half linewidths.). Standard absorption imaging is, however, not suitable for relatively dense clouds, because of the rapid saturation of the signal (standard absorption imaging can probe optical densities up to approximately 2 before saturation of the signal). The absorption imaging dynamic range can be increased, at the price of the sensitivity, by probing the cloud with highly saturated
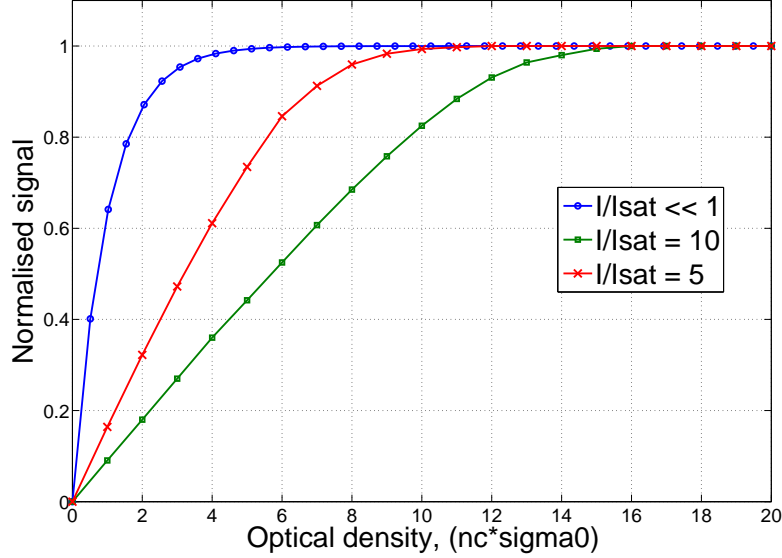
Figure 3.1: Absorption imaging signal, $|I_a - I_0|/I_0$, as a function of the optical density ($n_c \sigma_0$), for different saturation parameters s_0.

intensity as explained in Reinaudi et al. [13]. The column density n_c can be extracted from intensity measurements as

$$n_c = -\frac{1}{\sigma_0}\left[\ln\left(\frac{I_a}{I_0}\right) + \frac{I_a - I_0}{I_{sat}}\right], \tag{3.1}$$

where σ_0 is the resonant cross section, I_a the intensity measured in the presence of atoms, I_0 the intensity without atoms and I_{sat} the saturation intensity. Analytical inversion of Equation (3.1) is in general not possible in order to express the normalised signal $\frac{|I_a - I_0|}{I_0}$ as a function of the optical density OD $= n_c \sigma_0$. Numerical solutions are shown for standard and saturation absorption imaging in Figure 3.1. For *small* optical densities, the normalised signal S_{Abs} can be expressed as a linear function of the optical density,

$$S_{Abs} \approx \frac{n_c \sigma_0}{s_0 + 1} = \frac{\text{OD}}{s_0 + 1}, \tag{3.2}$$

where $s_0 = I/I_{sat}$ is the saturation parameter. Compared to standard absorption imaging ($I \ll I_{sat}$), saturation of the probe intensity reduces the signal of the method by a factor $s_0 + 1$ as can be seen in Figure 3.1. Thus, this permits an increasing of the optical density dynamics, approximately by a the same factor $s_0 + 1$ as can be seen in Figure 3.1.

3.1.2 Near-resonant phase contrast imaging

Saturation of the probe beam tends also to reduce the sensitivity of phase contrast imaging, but to a lesser extent than for absorption imaging. In the high saturation

regime, the phase contrast signal $S_{PCI} = \frac{|I_a - I_0|}{I_0}$ that follows from Equation (2.67) is given by

$$S_{PCI} = t^2 + 1 - 2t(\cos\phi + \sin\phi), \tag{3.3}$$

where ϕ is the phase shift caused by the atoms and t is the transmission coefficient of the cloud in the high intensity regime. Note that there is no analytical expression for t and ϕ in this regime. The transmission coefficient of the cloud is $t = \sqrt{\frac{I_f}{I_0}}$, where I_f is the intensity after the cloud and I_0 before. It can be numerically computed using the results of the last section that leads to the modified Beer-Lambert law,

$$\mathrm{d}I = -\frac{n\sigma_0}{1 + \delta^2 + I/I_{sat}} I \mathrm{d}z, \tag{3.4}$$

where n is the position-dependent density of the atomic cloud and I is the position-dependent intensity of the imaging beam. Relation (3.1) can be generalised to

$$n_c = -\frac{1}{\sigma_0}\left[(1 + \delta^2)\ln\left(t^2\right) + \frac{I_f - I_0}{I_{sat}}\right], \tag{3.5}$$

from which the transmission coefficient t can be numerically extracted.

The phase shift caused by the atoms follows from Equation (2.50),

$$\phi = -\frac{\sigma_0\delta}{2}\int_{-\infty}^{+\infty}\frac{n}{1 + \delta^2 + I/I_{sat}}\mathrm{d}z. \tag{3.6}$$

Integration of (3.4) and insertion of (3.6) leads to the atom phase shift,

$$\phi = \frac{\delta}{2}\ln t^2. \tag{3.7}$$

Again, we show in Figure 3.2 the effect of saturation on the phase contrast signal where we choose the optimal detuning for each saturation parameter. For *small* optical densities ($|\phi| \ll 1$ and $t \approx 1$), Equation (3.3) can be linearised,

$$S_{PCI} \approx -2\phi = n_c\sigma_0\frac{\delta}{1 + \delta^2 + s_0}, \tag{3.8}$$

where δ is the detuning in half linewidths. The maximal sensitivity is obtained when the derivative of Equation (3.8) with respect to δ is zero. The detuning that maximises the sensitivity of the signal in the linear regime is found to be

$$\delta = \sqrt{s_0 + 1}. \tag{3.9}$$

The dependence of the normalised signal with respect to the detuning is plotted in Figure 3.3. Substitution of (3.9) into (3.8) leads to the maximal sensitivity signal for phase contrast imaging,

$$S_{PCI} = \frac{\mathrm{OD}}{2\sqrt{s_0 + 1}}. \tag{3.10}$$
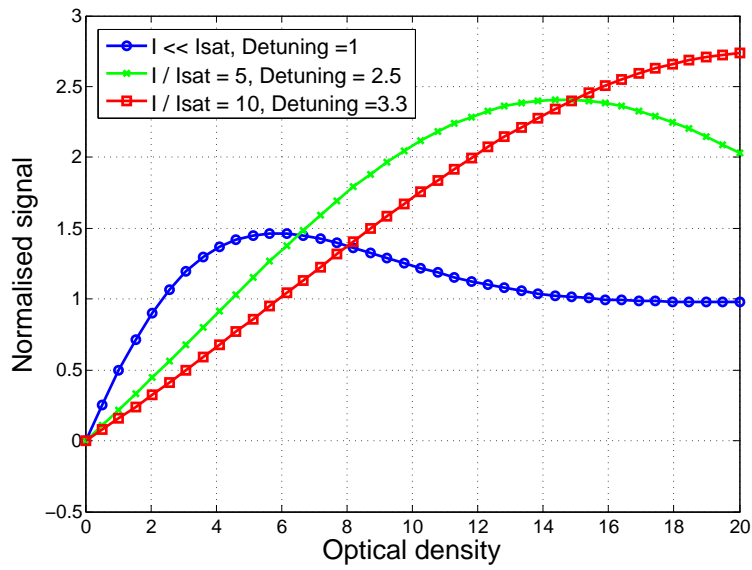
Figure 3.2: Phase contrast imaging signal for different saturation parameters s_0 and for the optimal detuning.
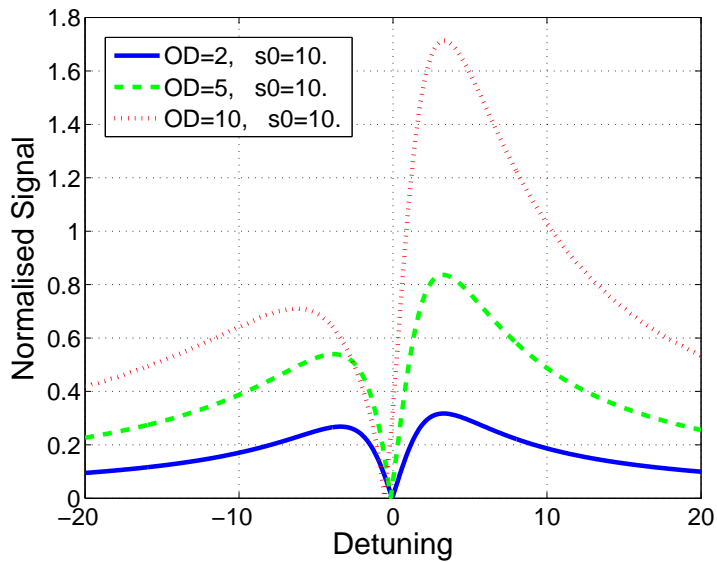

Figure 3.3: Normalised signal as function of the detuning for different optical densities. The signal is maximal for $\delta \approx \sqrt{s_0 + 1}$.
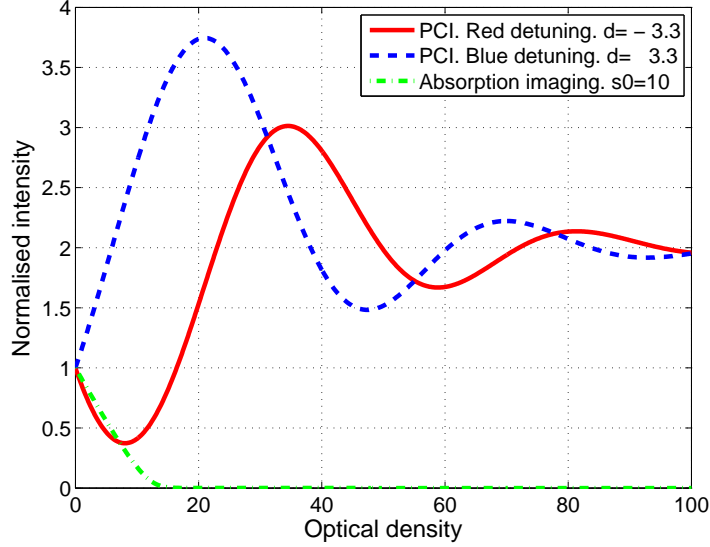
Figure 3.4: Normalised intensity (I_a/I_0) as a function of the optical density for different probe techniques. Phase contrast is performed with a $-\pi/2$ phase plate and $s_0 = 10$.

3.1.3 Comparison of the dynamic range

The dynamic range is the density range before the signal saturates. For saturation absorption imaging $(s_0 \gg 1)$, we showed that the dynamic in optical densities is roughly equal to $s_0 + 1$. For example, with a saturation parameter around $s_0 = 10$, it is possible to probe clouds up to OD ≈ 11. Beyond that density, the cloud is opaque.

Figure 3.4 shows the normalised intensity (I_a/I_0) as a function of the optical density for different probe techniques:

- optimal phase contrast imaging,

- phase contrast imaging with $-\pi/2$ phase plate and red detuned light,

- saturation absorption imaging.

The dynamic of the phase contrast technique is larger – for equivalent saturation– even if one does not considers the periodicity of the signal but just the domain before the first extremum of the signal. This statement is valid only if phase contrast imaging is performed in optimal conditions, for example with a $-\pi/2$ phase plate and blue detuned light.

3.1.4 Comparison of the normalised signal

As already mentioned, phase contrast has a larger dynamic range for any saturation regime because of the periodicity of the signal. We will now show that the sensitivity
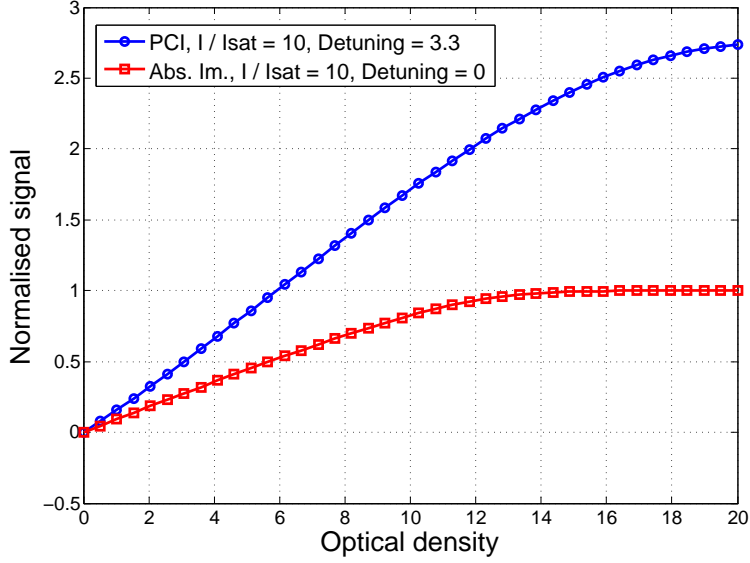
Figure 3.5: Normalised signal $\frac{|I_a - I_0|}{I_0}$ as a function of the optical density $n_c \sigma_0$ for both imaging techniques and for a typical saturation of $s_0 = 10$.

of phase contrast surpasses the one of absorption imaging for high probe intensities. Comparing the signals obtained with both techniques in the linear regime, the gain of near-resonant phase contrast versus absorption imaging can be expressed by the ratio

$$\frac{S_{PCI}}{S_{Abs}} = \frac{\sqrt{s_0 + 1}}{2}, \tag{3.11}$$

where we choose the detuning that maximises the sensitivity $\delta = \sqrt{s_0 + 1}$. This shows that optimal phase contrast imaging has a better sensitivity than absorption imaging for saturation parameters above $s_0 = 3$. For a typical experimental probe intensity of $I = 10 I_{sat}$, phase contrast imaging presents a signal stronger by at least a factor $\sqrt{11}/2 \approx 1.7$ as can be seen in Figure 3.5.

3.1.5 Signal-to-heating ratio

The quality of cold atoms images not only depends on the strength of the signal, but also on the noise present. Because the shot-noise-limited signal-to-noise ratio goes with the square root of the exposure time τ, long exposures are preferable. In probing cold atoms optically, however, the energy of the probe photons is not negligible compare to the kinetic energy of the atoms so that imaging free atoms is a destructive process, limiting the exposure time. The amount of signal collected per scattered photon or **signal-to-heating ratio** is then of great interest. We now show that phase contrast imaging is a less destructive technique than absorption imaging for a given exposure time.

For resonant absorption imaging, the scattering rate (2.56) reduces to

$$\Gamma_{Abs} = \frac{\Gamma}{2} \frac{s_0}{1 + s_0},$$
(3.12)

where Γ is the decay rate. For high saturation parameters, the scattering rate settles approximately to $\Gamma/2$. The scattering rate for the detuned light of optimal phase contrast imaging is less by a factor two due to the detuning (chosen to maximise the signal as seen in section 3.1.2),

$$\Gamma_{PCI} = \frac{\Gamma}{4} \frac{s_0}{1 + s_0}.$$
(3.13)

Near-resonant phase contrast imaging, being less destructive than absorption imaging, enables longer exposures as will be seen in the following Section 3.2. If we normalise the scattering rate to $\Gamma/2$ in order to deal with unitless quantities, Γ_{Abs} and Γ_{PCI} become

$$\Gamma'_{Abs} = \frac{s_0}{1 + s_0},$$
$$\Gamma'_{PCI} = \frac{s_0}{2(1 + s_0)}.$$
(3.14)

The signal-to-heating ratio S/Γ' defined as the ratio between the normalised signal and the normalised scattering rate is given for absorption and phase contrast imaging by

$$S_{Abs}/\Gamma'_{Abs} = \frac{OD}{s_0},$$
$$S_{PCI}/\Gamma'_{PCI} = \frac{OD\sqrt{s_0 + 1}}{s_0}.$$
(3.15)

For the same number of scattered photon, phase contrast delivers approximately $\sqrt{s_0 + 1}$ more signal.

3.1.6 Signal-to-Noise ratio

For small optical densities ($OD \simeq 0$), both techniques give about the same noise per unit time and the gain in SNR provided by phase contrast imaging with a longer exposure time $\tau_{PCI} > \tau_{Abs}$ is

$$\text{Gain}_{SNR} = \frac{S_{PCI}}{S_{Abs}} \sqrt{\frac{\tau_{PCI}}{\tau_{Abs}}}$$
$$= \frac{\sqrt{s_0 + 1}}{2} \sqrt{\frac{\tau_{PCI}}{\tau_{Abs}}},$$
(3.16)

where τ_{PCI} and τ_{Abs} are exposure times for phase contrast and absorption imaging, respectively. Because atoms imaged with the phase contrast technique[1] appear

---

[1] With a $-\pi/2$ phase plate and blue detuned light.
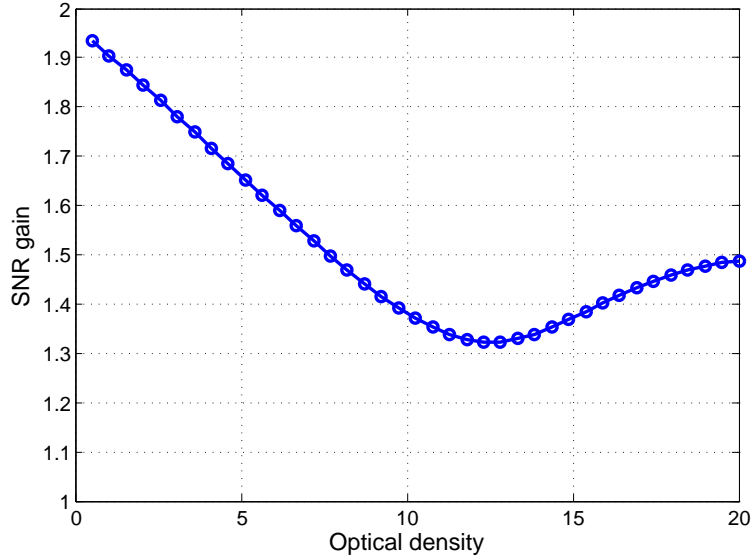
Figure 3.6: Gain on the SNR: SNR_{PCI}/SNR_{Abs} procured by phase contrast compared to absorption imaging with $\tau_{PCI} = 1.4\ \tau_{Abs}$ (see section 3.2.3).

brighter than the background, the shot noise associated to this signal is bigger than the shot noise associated to the absorption signal. In other words, phase contrast gives more signal than absorption imaging (3.16), but induces also more shot-noise. For increasing optical densities, it turns out that the gain in the SNR obtained by phase contrast decreases first, reaches a minimum and grows again, but never falls below unity as can be seen on the numerical calculation of Figure 3.6.

3.2 Imaging an expanding cloud

In the last section, we showed that the scattering rate during optimal phase contrast imaging is half that of absorption imaging and, therefore, phase contrast enables longer exposure. How much longer? In practice, the exposure time is chosen as long as possible such that no significant image degradation is observed. In this section, we want to investigate the possible sources of blurring that affect the image in order to understand what actually limits the exposure time.

3.2.1 Expansion of the cloud

During a typical exposure of 15 µs with saturated probe intensity, an atom undergoes hundreds of scattering event. The interaction of an atomic cloud with the probe beam can be divided in two processes that both tend to degrade the image quality[2]:

---

[2]Since atoms are initially *ultra cold*, we will neglect their initial thermal velocity compare to the velocity they acquire during the imaging. In order to facilitate the description of the cloud
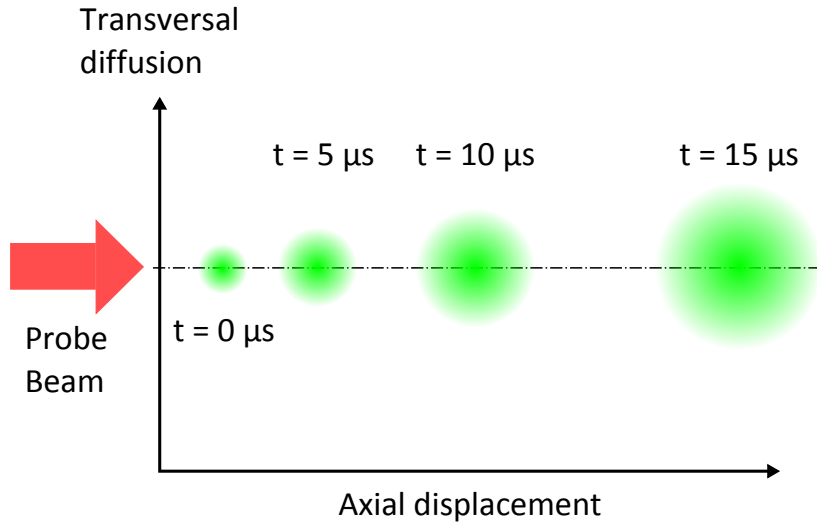
Figure 3.7: Schematic picture of the expanding cloud at regular time interval. The centre of mass of the cloud is pushed along the optical axis toward the objective and the cloud diffuses isotropically.

1. radiation pressure of the probe beam pushes the centre of mass of the cloud in the beam direction. Pushing the atoms out of focus introduces blurring and loss of signal.

2. the random re-emission of photons induces an isotropic diffusion of the cloud around the centre of mass. If the cloud's spatial extent exceeds the optical resolution limit, images may appear blurred.

Figure 3.7 shows schematically the expansion (axial displacement and isotropic diffusion) of an initially point like cloud during imaging.

Radiation pressure

Atoms pushed by the radiation pressure acquire, after a time Δt, an average velocity of $v_{rec}\Gamma_{sc}\Delta t$ along the probe beam propagation direction, where v_{rec} is the recoil velocity, Γ_{sc} is the scattering rate. After an exposure time of τ, the center of mass of the cloud has moved by the distance

$$\Delta z = v_{rec}\Gamma_{sc}\frac{\tau^2}{2}. \tag{3.17}$$

Typical displacement of the cloud during a 15 µs long exposure and with a saturated probe beam is around 13 µm for absorption and 6 µm for phase contrast imaging. The axial displacement effects can be reduced when the imaging system is set so

_____

expansion, we assume an initially point like cloud.

that, at the beginning, atoms are slightly out of focus and travel through the front focal plane of the objective (Muessel et al. [15]).

Note that, in practice, the probe beam is not perfectly aligned with respect to the optical axis but slightly tilted (by approximately 4° in our imaging setup) so that the atoms are additionally shifted laterally when observed from the objective. This lateral shift is approximately 1 μm under typical absorption imaging conditions.

Isotropic diffusion

The spontaneous re-emission of photons by the atoms leads to a spatial Gaussian diffusion of the cloud. The standard deviation σ_{cloud} of the Gaussian profile can be derived from the atom's random walk in velocity space (Joffe et al. [16]),

$$\sigma_{cloud} = \frac{v_{rec}}{3}\sqrt{\Gamma_{sc}}\tau^{3/2}. \tag{3.18}$$

Typical radial extents of the cloud are $2\sigma = 0.6\,\mu\text{m}$ for absorption and $2\sigma = 0.4\,\mu\text{m}$ for phase contrast imaging after an exposure of 15 μs.

3.2.2 Imaging an expanding cloud: the "Cloud Spread Function" (CSF)

In the last section, we saw that during the imaging process, the atomic cloud is pushed towards the objective and diffuses slightly. These effects can be substantial for the image quality if the objective has a shorter depth of field than the axial displacement of the cloud and a diffraction limited resolution comparable to the spatial diffusion of the cloud and the lateral shift. In this section, we develop a model to describe, in a simple way, the imaging of such an expanding cloud.

The image of a moving scene is an integration of the time-dependent intensity falling on the CCD during the exposure time:

$$\text{Image} \propto \int_0^\tau I(t)\mathrm{d}t \tag{3.19}$$

where the image can be express in photon/m^2 or in counts/pixel. We now make an approximation (that is reasonable considering the particular object we want to image) by describing the imaging process using incoherent imaging theory rather than the coherent theory. In contrast to coherent imaging, incoherent imaging is a linear mapping of intensity so that the intensity in the image plane of an optical system is given by

$$I_{im} \propto |PSF|^2 * I_{obj}, \tag{3.20}$$

where I_{im} and I_{obj} are the intensities in image and object plane respectively, PSF is the point spread function of the system and $*$ denotes the two-dimensional convolution product. In our case, the incoherent imaging theory is expected to give

satisfying result because we image an array of well separated, microscopic, bell shaped clouds. Furthermore, incoherent imaging enables a more concise and intuitive description of the imaging of moving objects. Inserting Equation (3.20) into (3.19) leads to

$$\text{Image} \propto \int_0^\tau |PSF(t)|^2 * I_{obj}(t)\mathrm{d}t, \tag{3.21}$$

where $I_{obj}(t)$ is the intensity in the plane orthogonal to the optical axis and containing the centre of mass of the cloud, this plane is called the *defocused plane*. $I_{obj}(t)$ carries information on the isotropic diffusion of the cloud. $PSF(t)$ is the point spread function associated to the defocused plane; it includes diffraction of the optical system and blurring due to defocusing of the centre of mass. Therefore, $PSF(t)$ is the response of the system to a defocused point source in object space and will now be denoted $DPSF(t)$ for *Defocused Point Spread Function*(see Chapter 6 of Goodman [4]). The intensity in the defocused plane $I_{obj}(t)$ can be written as a convolution product: $I_{obj}(t) = I_{obj}(0) * G(t)$ where $G(t)$ is a Gaussian function describing the transversal spatial diffusion of the cloud and $I_{obj}(0) = I_{obj}(t = 0)$ is the initial intensity profile of the cloud. Using the linearity of the convolution product, the image delivered by the camera can be written as a convolution product,

$$\text{Image} \propto I_{obj}(0) * \underbrace{\int_0^\tau |DPSF(t)|^2 * G(t)\mathrm{d}t}_{\text{Cloud Spread Function}}. \tag{3.22}$$

The time integral of Equation (3.22) is a real function of the exposure time τ, that once convolved with the initial intensity profile gives the actual image delivered by the camera. We call this the **Cloud Spread Function** (CSF), because it generalises the concept of point spread function for an expanding cloud. The intuitive meaning of the CSF is the following: it is the response to the imaging system to a point like expanding cloud. The peak value of the CSF is proportional to the amount of signal collected by the camera. The spatial spread of the CSF provides information about the total blurring affecting the images. The four main sources of blurring are the defocussing of the centre of mass due to radiative pressure, the diffraction of the system, the lateral shift due to the tilt of the probe beam, and finally the Gaussian transversal diffusion.

The actual image delivered by the camera is, in full analogy to the incoherent imaging theory, a convolution of the ideal intensity profile with an impulse response, the CSF,

$$\text{Image} \propto I_{obj}(0) * CSF(\tau). \tag{3.23}$$

3.2.3 Limitation of the exposure time

Because the atoms are moving during imaging, the exposure time has to be limited so that no significant blurring affects the images. We will now make use of the Cloud
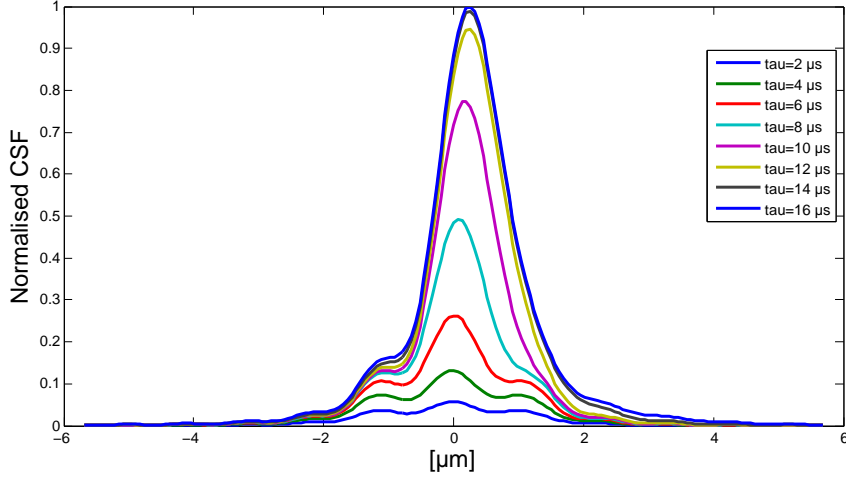
Figure 3.8: Cut of the cloud spread function for growing exposure time τ. The case considered here is absorption imaging with $s_0 = 10$ and an initial defocus of $5\,\mu$m. The spatial coordinate is scaled with respect to the object space and has to be compared with the optical resolution limit of $1.1\,\mu$m and the interwell distance of $5.7\,\mu$m.

Spread Function in order to understand what actually limits the exposure time for absorption and phase contrast imaging.

The CSF is plotted in the case of absorption imaging, for a saturation parameter of $s_0 = 10$ and for an initial defocus of $5\,\mu$m in Figure 3.8.

The cloud spread function increases monotonically with the exposure time. However, the peak value of the CSF saturates after approximately $14\,\mu$s meaning that no useful signal is collected after this time. The width of the CSF, which is directly related to the spatial resolution, is near the diffraction limit of $1.1\,\mu$m. Thus, there is no considerable loss of resolution because of the expanding cloud. The reason why the exposure time has to be smaller than a certain value around $14\,\mu$s is that no significant signal is collected beyond that, but the noise increases. This phenomenon results from the atomic cloud escaping rapidly from the region of sharp imaging (within the depth of field) and being imaged in the form of a diffuse, weak halo contributing to the local background (the wings of the CSF). This can be seen by analysing the DPSF in Figure 3.9, which is the main contributor to the CSF. Note furthermore that, as expected from the tilted probe beam, the CSF travels laterally by a fraction of a micrometre.

Because we start the image acquisition with atoms slightly out of focus, the DPSF grows in the first $10\,\mu$s until atoms cross the front focal plane of the objective. After approximately $14\,\mu$s, atoms are beyond the depth of field and are imaged in the form of a diffused halo (red lower curve in Figure 3.9).

Phase contrast imaging offers the possibility to expose longer because of the lower scattering rate. The same analysis can be performed for near-resonant phase contrast
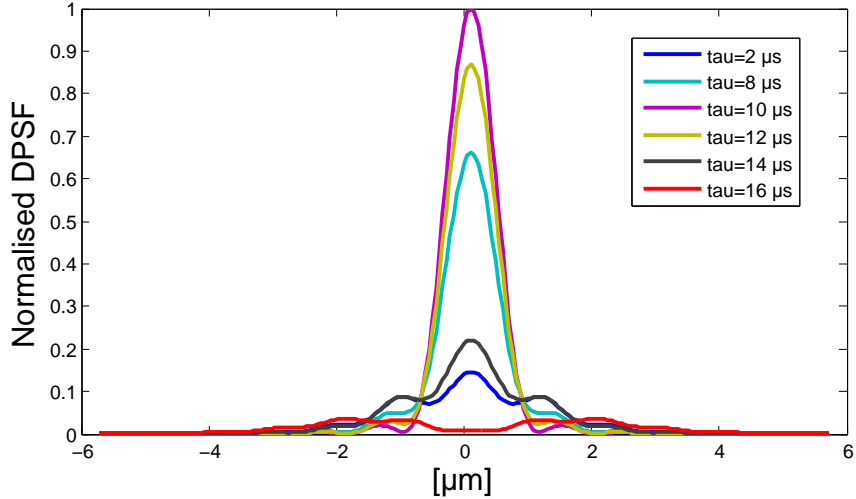
Figure 3.9: Cut of the DPSF for different exposure time τ in object space coordinate. The case considered here is absorption imaging with $s_0 = 10$ and an initial defocus of $5\,\mu m$. The DPSF grows when approaching the front focal plane reaches its maximum there after $10\,\mu s$ and vanish rapidly after $16\,\mu s$.

imaging. We find out that the saturation of the CSF appears later so that the maximal exposure time is around $20\,\mu s$ as can be seen in Figures 3.10 and 3.11.

Near-resonant phase contrast imaging enables approximately 40% longer exposure than absorption imaging.

3.3 Imaging simulations

After having compared the ideal cases of absorption and phase contrast imaging in Section 3.1, we considered in Section 3.2 the mechanical effect of the probe beam on the atoms. In the following section, we investigate further practical issues of imaging. For this purpose, we developed a code that accurately simulates the optical system in the lab which is a two *component* optical system. The first component is a high numerical aperture objective that collimates the object wave. The second component is an achromatic doublet with $1\,m$ focal length. The overall system has a magnification of -31.

3.3.1 Simulation scheme of a two-lens imaging system

Phase contrast and absorption imaging optical systems differ only by the presence or absence of a phase plate in the Fourier plane of the setup. It is therefore possible to simulate both techniques with the same simulation scheme as depicted in Figure 3.12.
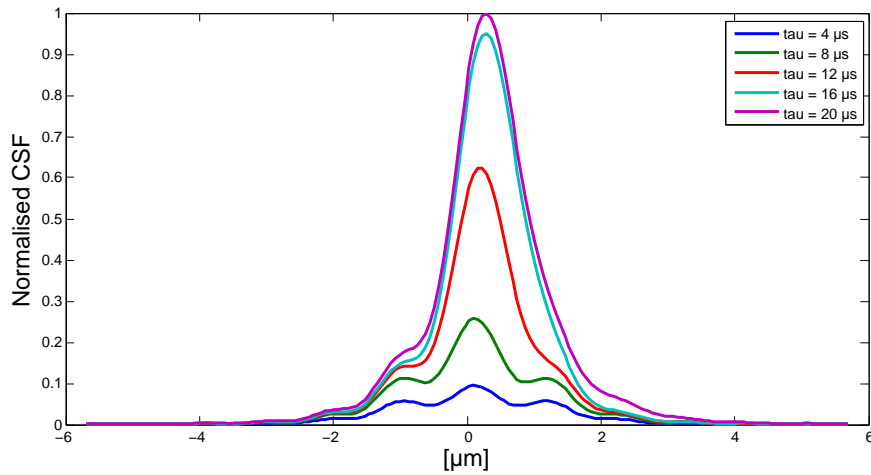
Figure 3.10: Cut of the Cloud spread function for growing exposure time τ in object space coordinate. The case considered here is phase contrast imaging with $s_0 = 10$, a detuning of $\delta = 3.3$ and an initial defocus of $5\,\mu m$. The CSF saturates after $20\,\mu s$.
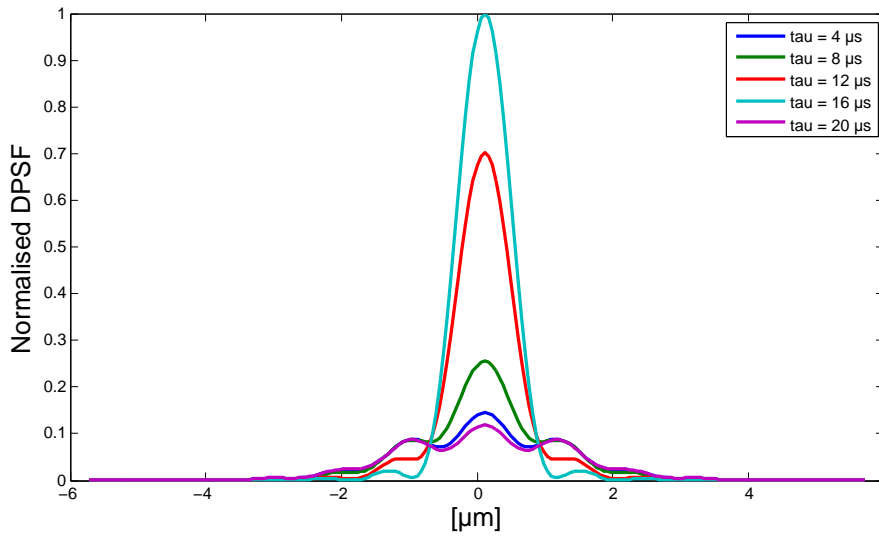

Figure 3.11: Cut of the DPSF in object space for different exposure time τ. The case considered here is phase contrast imaging with $s_0 = 10$, a detuning of $\delta = 3.3$ and an initial defocus of $5\,\mu m$. The DPSF grows when approaching the front focal plane, reaches its maximum there after approximately $16\,\mu s$ and vanishes rapidly after $20\,\mu s$.
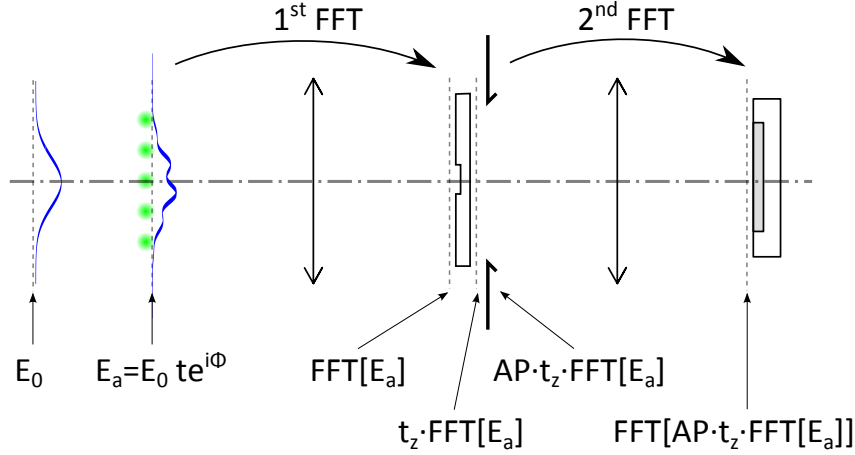
Figure 3.12: Simulation scheme of a two-lens optical system. The amplitude in the image plane is obtained by means of successive transmission coefficient multiplication and two Fourier transformations.

The main steps of the imaging simulation are the following:

1. We first define the probe beam properties: amplitude $E_0(x, y)$, wavelength λ, detuning δ. In practice, E_0 has a Gaussian profile.

2. The amplitude after the object is determined from the transmission coefficient and phase shift of the object so that: $E_a = E_0 t e^{i\phi}$.

3. The objective performs a Fourier transformation computed with the *Fast Fourier Transform* algorithm (FFT) so that the amplitude in the focal plane of the objective is $FFT[E_a]$.

4. The effect of the Zernike phase plate is implemented by multiplying the previous amplitude with the complex transmission coefficient of the Zernike phase plate t_z (see Appendix A). After the phase plate, the amplitude is $t_z \cdot FFT[E_a]$. In the case of absorption imaging, the Zernike phase plate is absent so that t_z is set to unity.

5. We now *a posteriori* take into account the finite extents of the lenses and define the aperture stop right after the phase plate[3]. The amplitude after the aperture stop is $t_z \cdot FFT[E_a]$ multiplied by the stop function AP which is unity inside the (circular) aperture and 0 outside.

6. The amplitude on the camera is obtained by means of a second Fourier transform. The amplitude on the camera is then $FFT[AP \cdot t_z \cdot FFT[E_a]]$ from which we can infer the intensity.

---

[3]Because the object beam is collimated after the objective we have the freedom to position the aperture stop where ever we want between the objective and the imaging lens.

44
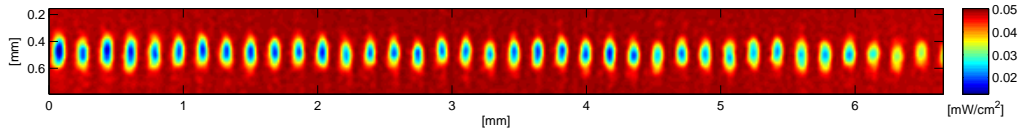
(a) Absorption imaging.
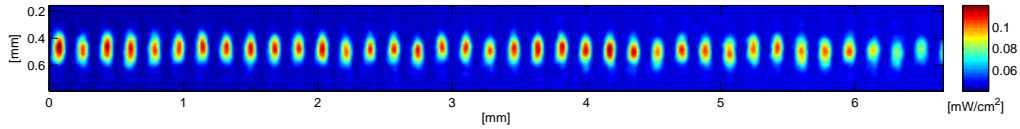

(b) Phase contrast imaging

Figure 3.13: Imaging simulations for both techniques. Each well contains approximately 600 atoms. $s_0 = 18$. The detuning for phase contrast imaging is 4.4 half linewidths.

We show in Figure 3.13 results of simulations for phase contrast and absorption imaging under typical experimental conditions. As an object, we use a real column density profile measured in the lab. Absorption imaging records the shadow of the atoms such that atoms appear darker than the background. In contrast, phase contrast imaging performed with blue detuned light and a negative phase shift $\left(-\frac{\pi}{2}\right)$ delivers a positive signal.

3.3.2 Diffraction effects

The implementation of phase contrast imaging on the existing optical setup will imply, as will be seen in Chapter 4, a smaller aperture stop. We now want to investigate the effect of a reduced aperture stop on the quality of clouds images.

We then simulated phase contrast imaging for varying size of aperture stop and results are shown in Figure 3.14. The individual clouds look well separated for aperture stops greater than approximately 10 mm. A significant overlap of the clouds is observed for apertures smaller than 9 mm. Interference features such as the fringes superimposed with the clouds shown in Figure 3.14(e) can not be understood in the framework of incoherent imaging. They result from interferences between adjacent clouds.
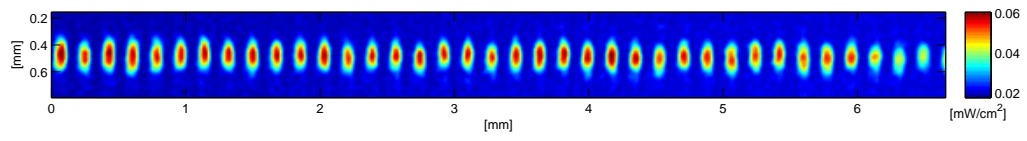
(a) 28 mm aperture stop.
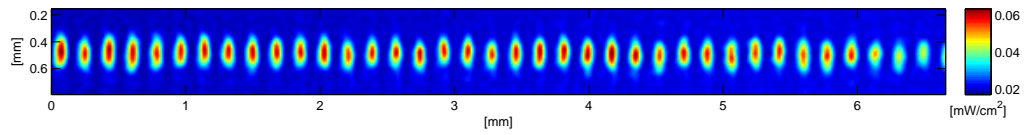
(b) 23 mm aperture stop
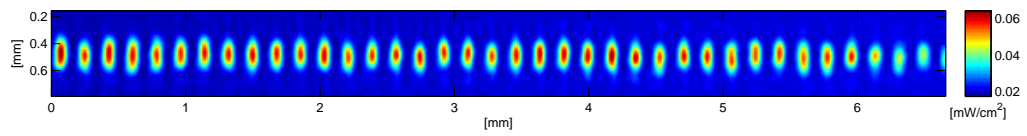
(c) 18 mm aperture stop
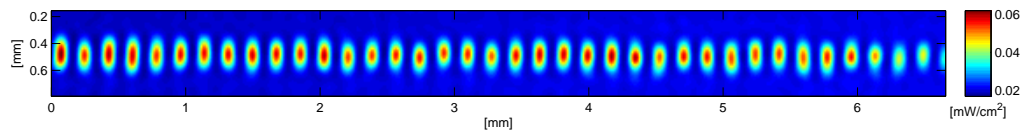
(d) 13 mm aperture stop
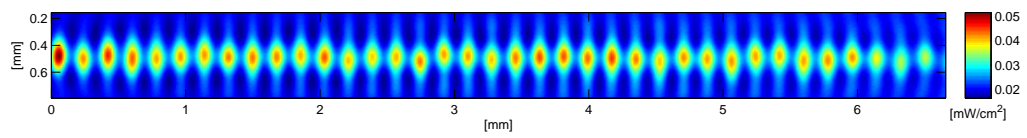
(e) 9 mm aperture stop
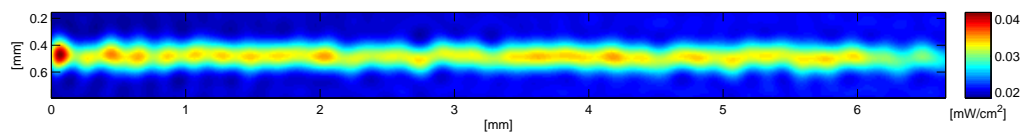
(f) 8 mm aperture stop

Figure 3.14: Simulation of phase contrast pictures of atoms for different aperture stop diameters.

3.3.3 Defocus effects

Diffraction and interference effects have to be suppressed, not only because they limit the resolution, but also because they complicate the density profile extraction by adding features to the image that do not exist in the real density profile.

These effects are more pronounced in the presence of defocussing (we mean here an average defocussing over the exposure time). For this reason, we investigate here the effect of defocussing on the atom pictures. It is possible to implement defocussing in the simulation scheme of Figure 3.12 by letting the object wave E_a expand in free space before performing the first FFT. We used here the results of Section 2.1.3.

Talbot Effect

Defocussing enables the observation of an interesting phenomenon, called the Talbot effect, that occurs in the near field of a diffraction grating. It consists of the reproduction of the grating structure after a certain distance called the Talbot length: $\frac{2p^2}{\lambda}$ (78 µm in our case) where p is the period of the grating (5.5 µm in our case). At half the Talbot length (39 µm defocus), the grating structure is also reproduced, but inverted, as can be seen in Figure 3.15.

3.3.4 Defocus effect for other objects

The effect of the defocussing depends strongly on the particular object of observation. Indeed, objects that exhibits sharp edges are more likely to exhibits interferences effects due to defocussing. We now want to investigate how different object structures (a Gaussian profile, a parabolic and a square profile) appear in image space with a slight defocussing of the objective. We start our simulations with an elongated cloud as an object, that exhibits the desired profile in the vertical direction (i.e. square, parabolic or Gaussian). The widths of these profiles are comparable to the typical clouds created in the lab (around 3 µm). Results are presented in the form of cuts in the vertical direction, instead of as full two dimensional images, for a better visibility. Results are shown in Figure 3.16.

(a) On focus

(b) 10 µm defocus.

(c) 20 µm defocus.


(d) 30 µm defocus.
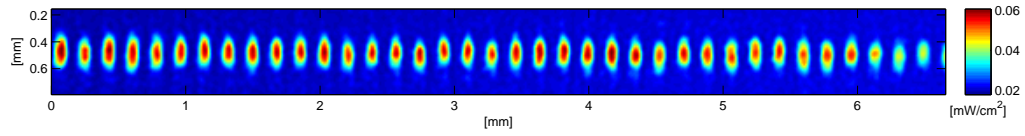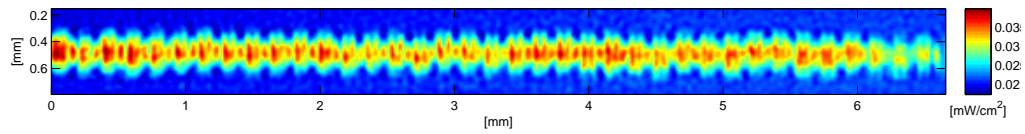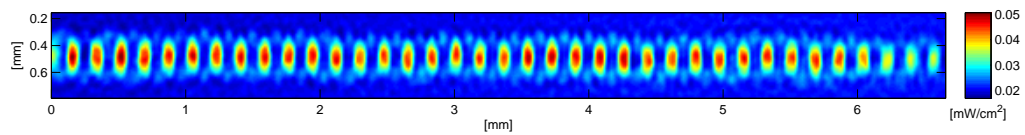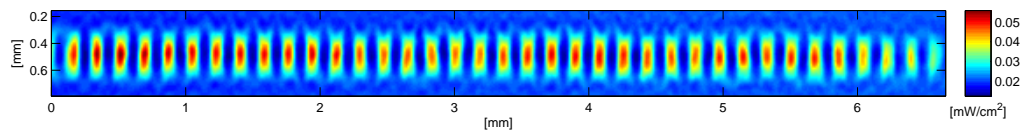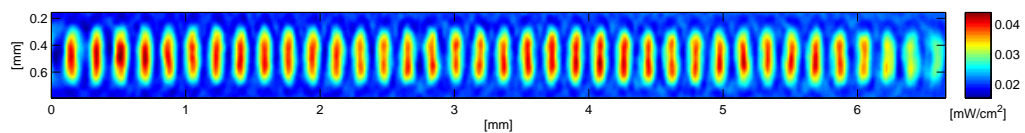
(e) 40 µm defocus.

Figure 3.15: Simulation of phase contrast pictures of atoms for increasing defocus. For a defocussing equivalent to half the Talbot length (around 40 µm), the atomic density profile is reproduced and inversed (atoms are seen where they are absent in fact).

(a) Square profile in focus.

(b) Square profile 4 µm defocused.

(c) Square profile 8 µm defocused.

(d) Parabolic profile in focus.

(e) Parabolic profile 4 µm defocused.

(f) Parabolic profile 8 µm defocused.

(g) Gaussian profile in focus.

(h) Gaussian profile 4 µm defocused.

(i) Gaussian profile 8 µm defocused.
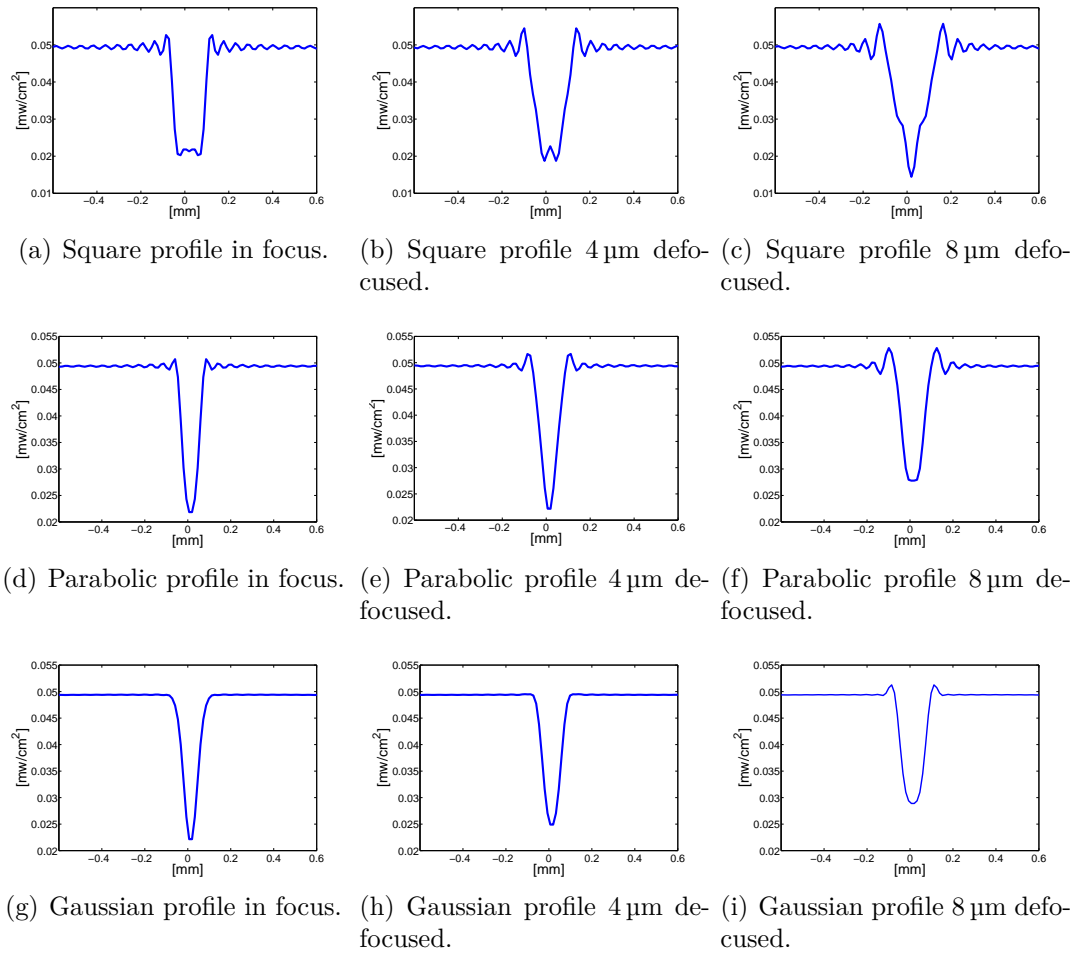
Figure 3.16: Effect of a slight defocus on absorption images for different object structure. The first row corresponds to a square object profile, the second row to a parabolic object profile, and the third to a Gaussian profile.

Defocus tends to amplify the typical interference fringe pattern at the edge of the structures. Structures that present sharp edges (square profile) are strongly altered in the presence of a slight defocus. In contrast, for an equivalent width, the Gaussian profile, that has smooth edges, is less altered by defocussing.

It is possible that, because defocus affects the parabolic profile more than the Gaussian profile, it can be used to get information on the interaction regime of a Bose-Einstein condensate even if the cloud is not optically resolved. Indeed, in the non-interacting regime and at zero temperature, the density profile of a BEC in an harmonic trap is Gaussian. In the Thomas-Fermi limit, the density profile is an inverted parabola (see chapter 10 and 11 of Pitaevskii and Stringari [17]).

4 Implementation of phase contrast imaging

In the last section, we showed that phase contrast imaging, when performed near-resonant, could present some advantages over absorption imaging for the observation of mesoscopic BECs. In the following section, we first report on the design of the phase contrast system, beginning with the most crucial component: the phase plate. We then present how we managed to implement phase contrast as a flexible tool in the existing absorption imaging system. Finally, we present our first phase contrast images and report on a first attempt to calibrate the system.

4.1 The phase plate

4.1.1 Phase plate specifications

Phase plate structure

The maximum phase contrast sensitivity can be obtained with a phase plate that either **advances** ($-\pi/2$ phase shift) or **retards** ($+\pi/2$ phase shift) the unscattered light by $\pi/2$ compared to the object wave. The maximal dynamics before the signal reaches his first maximum and rolls over is obtained either with a retarding phase plate and red-detuned light or with a phase plate that advances the phase and blue-detuned light.

There is no obvious advantage of one option over the other except practical manufacturing considerations. A retarding phase plate is achieved by having a small bump onto the substrate. In contrast, an advancing phase plate requires a small dip in the substrate as presented in Figure 4.1. As will be reported in section 4.1.2, we investigated both possibilities but since the later design 4.1(b) was finally preferred, we assume up to now that we deal with an advancing phase plate.

(a) Retarding phase plate.   (b) Advancing phase plate.

Figure 4.1: Schematical representation of the two possible phase plate design.

Dip depth. Introducing a phase shift $\Delta\varphi$ requires a dip with depth e given by

$$e = \frac{\lambda}{2\pi(1-n)}\Delta\varphi, \tag{4.1}$$

where λ is the probe beam wavelength and n is the refractive index of the substrate. For a negative phase shift of $-\pi/2$, the depth is

$$e = \frac{\lambda}{4(n-1)}, \tag{4.2}$$

which is around 430 nm for silica glass and for the probe beam wavelength of 780 nm.

Dip diameter. Because we want to phase shift only the unscattered light without disturbing the object wave, the dip size has to be as small as possible. Nevertheless, the minimal dip diameter is limited by the size of the focused probe beam which has to fit entirely in the dip. Additionally, it is preferable to allow for some space in order to facilitate optical adjustments. For a typical focused probe beam diameter around 20 µm, a dip diameter of 100 µm seamed to be a good compromise.

Phase plate substrate.

The substrate has to be carefully chosen so that the phase plate does not introduce significant distortion to the object wavefronts.

Substrate diameter. The clear aperture of the phase plate has to be equal or superior to the *collimated* object wave with diameter 28 mm. This enables to exploit the full numerical aperture of the objective and the best resolution.

Surface flatness. According to Maréchal's criterion (See chapter 9 of Born and Wolf [5]), an optical system is *well corrected* if the RMS wavefront distortion is less than $\lambda/14$. We then charge the phase plate to fulfil Maréchal's criterion.

Substrate. We found a standard optical window of Newport (Model: FSW16) that meets quite well the substrate requirements. Details of the Newport uncoated window are listed in table 4.1.

The complete specifications sent to the manufacturer **HOLOEYE** can be consulted in appendix B. After agreement on the contract we sent a substrate to Holoeye that manufactured the phase plate within five weeks. At the reception, we only had to deplore a slight 1 mm long scratch on one surface, without practical consequences. The dip appears with bear eyes as a dust point.

Material	Fused silica
Refractive index	1.45 at 780 nm
Diameter	30 mm
Clear aperture	24 mm
Wavefront distortion	$\lambda/12$ at 780 nm
Thickness	4 mm
Parallelism	$< 5''$

Table 4.1: FSW16 specifications.

4.1.2 Alternative phase plates

Manufacturing an advancing phase plate is commonly done by etching the dip in the substrate. It is clear that etching is more suited for manufacturing advancing phase plates 4.1(b) than retarding phase plates because there is less matter to dig off. This technique is well established although expensive and already successfully produced phase plates with comparable specifications (Meppelink et al. [8], Sadler [18]).

Retarding phase plates of the type 4.1(a) can be manufactured by the deposition of a thin film of dielectric onto the substrate previously prepared and covered with a drilled mask. This sputtering technique was used by Haljan [19] to produce *cheap* home-made phase plates.

We also note that phase contrast imaging can be advantageously performed with an absorbing phase dip/bump in order two lower the back ground level and thus increase the contrast as already mentioned by Zernike [20]. In the appendix A we show that the signal to noise ratio is not affected by the absorbing phase plate. This particular phase plate could be of interest in the in-situ far detuned phase contrast regime where saturation of the camera is the limiting factor.

4.1.3 Characterisation

We would like to test if the phase plate manufactured by HOLOEYE fulfils our main specifications. We present here the technique used in order to quantitatively check the phase shift and the size of the dip as well as to qualitatively evaluate the overall surface finish and dip structure.

Measuring the depth of the dip e and knowing the index of refraction n of the substrate leads with Equation (4.1) directly to the phase-shift $\Delta\varphi$ at any given wavelength λ,

$$\Delta\varphi = \frac{2\pi}{\lambda}e(1-n).\tag{4.3}$$

Microscopes with nanometre depth resolution and micrometer lateral resolution such as an atomic force microscope or a confocal microscope would have done the job perfectly. A more economical alternative is a home build interferometer. We chose

the typical Mach-Zehnder configuration where we implemented an optical system to image the phase plate on a CCD camera as seen in Figure 4.2.

Advantageously, the interferometric methods give directly the phase shift for a given wavelength without calling on Equation (4.3).

Let U_{pp} be the complex amplitude just after the phase plate and U_0 be the complex amplitude on the reference beam. If we build the imaging system so that the planes containing U_{pp} and U_0 are conjugated with the CCD chip, the camera records the interferences between U_0 and U_{pp}:

$$I_{CCD} \propto |U_0 + U_{pp}|^2$$

and enable the phase shift determination[1].

Dip diameter measurement

If the two interferometer beams are well superposed[2] on the second beam splitter, we are in the *flat field* configuration and the phase dip appears as a homogeneous patch as seen in Figure 4.3.

Considering the magnification of the imaging system of 2.5 and the pixel size of $8.6\,\mu\mathrm{m} \times 8.3\,\mu\mathrm{m}$, we found the diameter of the dip to be $103(3)\,\mu\mathrm{m}$, which is in good agreement with the specifications $(100\,\mu\mathrm{m})$.

Phase-shift measurement

A slight misalignment[3] of the two interfering beams causes rectilinear fringes to appear, as seen in Figure 4.4. The fringes gives a direct information about the depth profile of the phase plate using the equivalence: 2π phase shift $\Leftrightarrow$ 1 fringe period.

In order to accurately determine the phase shift, we implemented a numerical routine to analyse interferograms:

---

[1]Note that in principle, interferences are also seen without imaging system. But in this case, we observe the interference of the two fields located directly on the second beam splitter and not the field of interest located just after the phase plate. In our case, the strong diffraction on the small circular phase dip causes the complex amplitude to lose its precious phase information before reaching the beam splitter. An imaging system enables to address any plane (complex amplitude) of interest within the interferometer.

[2]Superpose means here that the wavefronts of the two interfering waves emerges parallel to each other and that the beams are overlapped.

[3]Misalignment means here that the wavefronts of the two interfering waves do not emerge parallel anymore. We would like to give here an experimental tip: misalignment can be introduced at three different locations in the interferometer: at each mirror and at the second beam splitter. Introducing misalignment with the beam splitter is the best option because it keeps the interferometer configuration untouched for different misalignment, i.e. for different fringe configuration. Contrariwise, introducing the misalignment with the mirror of the phase plate arm causes the probe beam not to fall perpendicularly on the phase plate and introduces shadow effects near the dip edges (see the interferogram of Figure 4.4).
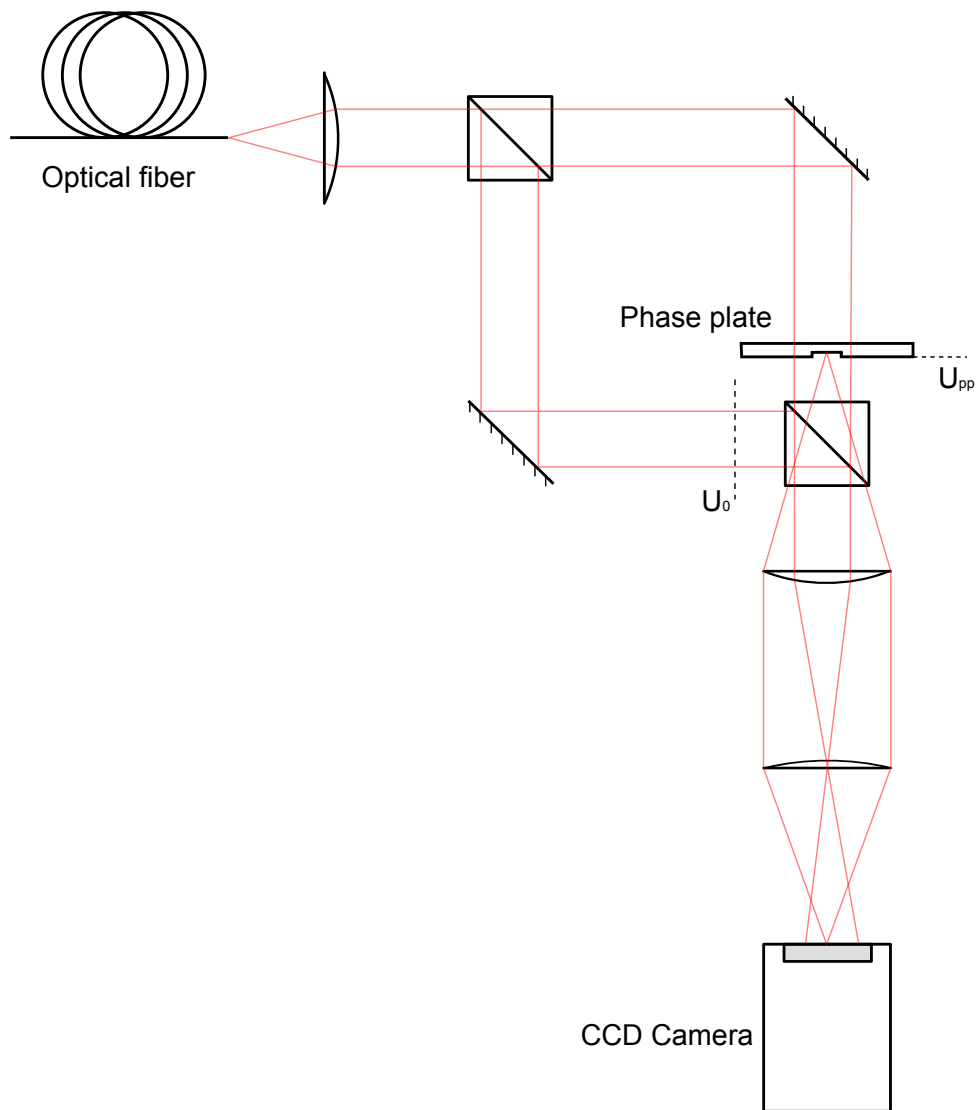
Figure 4.2: Phase plate characterisation using the Mach Zehnder interferometer.
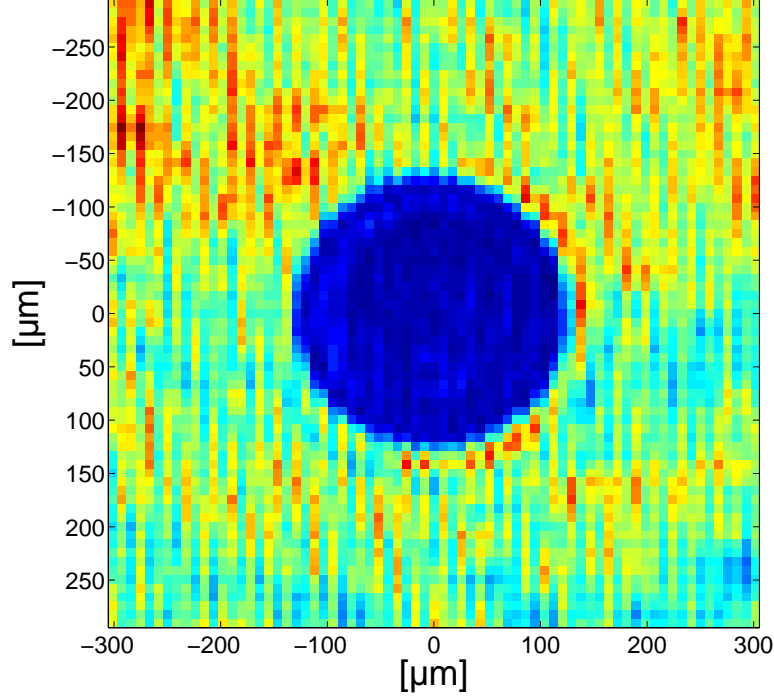
Figure 4.3: Flat field interferogram of the phase plate.

- In the external region around the dip, we fit the signal with a two dimensional sinusoid. Among the multiple fitting parameters, we record the phase of the external sine function.

- We do the same for the internal region within the Dip and record the phase of the internal sine function.

- We calculate the phase difference of the two sine function which is also the wanted phase shift[4].

The average measured phase shift for various fringe inclination is $-1.63(8)$ rad at a wavelength of 780.24 nm which is fully consistent with our specifications ($-1.57(10)$ rad).

---

[4]Assuming a flat surface and an homogeneous illumination in each region, the fit function for the fringes pattern is:

$$f_{ext/int}(x, y) = A \sin \left[2\pi (f_x x + f_y y) + \varphi_{ext/int} \right] + C$$

where A is the amplitude of the fringes, f_x and f_y are the spatial frequencies, $\varphi_{ext/int}$ the phase at the origin for the external/internal region and C is the overall offset. The phase shift is simply : $\Delta\varphi = |\varphi_{ext} - \varphi_{int}|$. The accuracy of the phase determination increases with the spatial frequency of the fringes but is limited by the finite pixel size, i.e. pixel resolution. With our camera, a good compromise is a period comprised between 50 and 100 µm. Note that the phase shift is wavelength dependant: $\Delta\varphi(\lambda) = \frac{\lambda_m}{\lambda} \Delta\varphi_m$ where λ_m refers to the wavelength used for the phase shift determination $\Delta\varphi_m$.
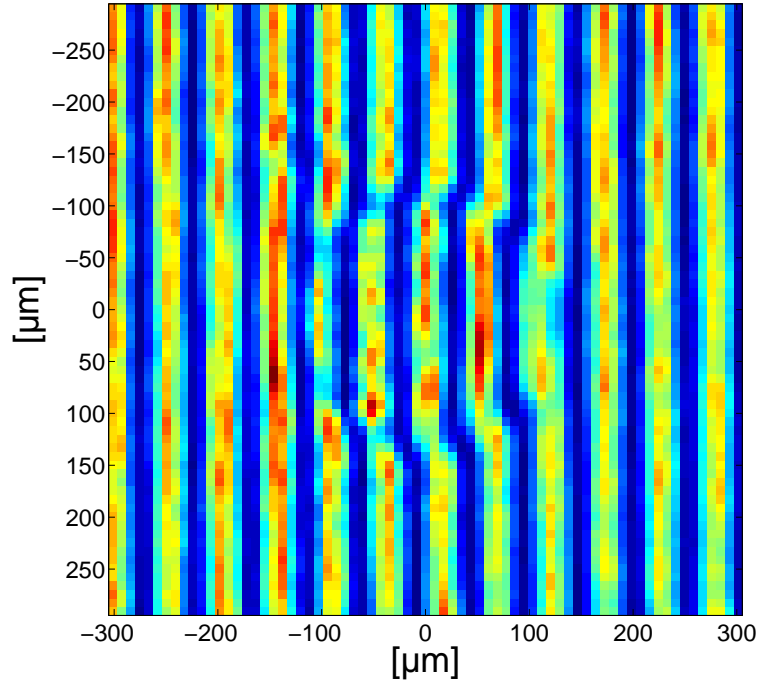
Figure 4.4: Fringe interferogram of the phase plate.

Surface finish and overall dip structure

As seen from the flat field interferogram of Figure 4.3, the dip shows a smooth surface, well pronounced edges[5] as well as the wanted circular geometry.

4.2 Optical and optomechanical system

4.2.1 Existing optical system

We aim to implement phase contrast imaging to the existing absorption imaging setup shown in Figure 4.5. The final system should enable both imaging techniques to run independently. Because the back focal plane of the objective lies within the objective mount (see Figure 4.6), access is limited for building in a phase plate. We overcame this issue by using a 1:1 relay telescope[6] in order to transfer the Fourier plane to an accessible place. The system consisting of the telescope and the phase plate should be able to be moved freely in and out of the existing setup to performed

---

[5]The slight concentric ring pattern around and inside the dip as well as the inhomogeneous field illumination come from residual diffraction on the dip. This can shown experimentally by slightly moving the phase plate and observing that this pattern is not following the plate surface.

[6]A one to one telescope has the advantage of giving the same magnification for both imaging techniques.

200 mm

Figure 4.5: Optical system for performing absorption imaging. The objective is a three lens system designed by Zeiss with numerical aperture NA=0.45 and 31.23 mm focal length. The imaging lens is a standard doublet of 1 m focal length. The effective magnification is -31.

Atoms

Glass cell

Back focal plane
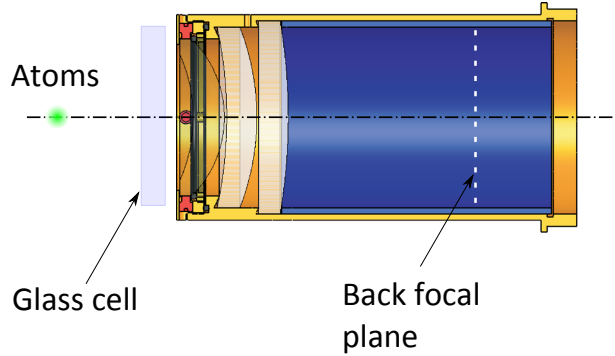
Figure 4.6: Objective of the BEC experiment. Details on the objective can be found in the thesis of Ottenstein [21].

the desired imaging.

4.2.2 Relay system

Considering the space constraints between the objective mount and the imaging doublet, the biggest 1:1 telescope that fits in is made of two lenses with 100 mm focal length. We avoid using shorter focal length because, for a given diameter, fast lenses introduce more aberrations. Ideally, we would like to use lenses with diameter larger than the image-forming pencil emerging out of the objective (28 mm) in order to exploit the full resolution of the system. Optical simulations with Oslo showed, however, that large standard doublets with diameter greater than 28 mm lead to a resolution that is worse than for 25 mm standard doublets. This is because larger lenses are more subject to aberrations. We finally decided in favour of two achromatic doublets from Newport with 25 mm aperture (and 23 mm clear aperture) and 100 mm focal length (**Model PAC12AR.16**). The PCI optical setup is shown in Figure 4.7 considering the object rays and in Figure 4.8 considering the probe beam. It consists of the original absorption imaging system with the inserted relay telescope and the phase plate. Note that the probe beam is tilted by approximately 4° with respect to the optical axis in order to prevent interference fringes from the glass cell.
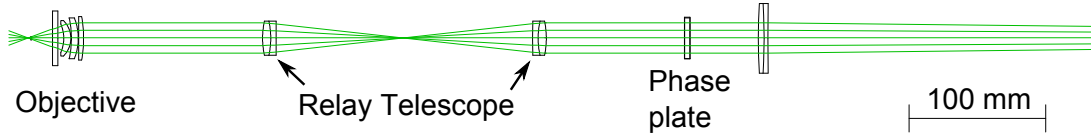
Figure 4.7: Phase contrast optical system consisting of the combination of the existing setup, the relay telescope and the phase plate.
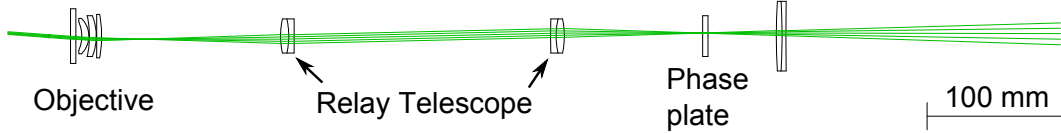
Figure 4.8: Propagation of the probe beam in the phase contrast imaging setup. Note the inclination of the probe beam by 4°.

4.2.3 Optical performance

Because the telescope reduces the size of the aperture stop of the system ($23\,\text{mm}$ instead of $28\,\text{mm}$) and introduces slight aberrations, the resolution of the system is going to be affected. We used the optics software Oslo to evaluate the loss of resolution due to the telescope.

The original absorption imaging setup is a diffraction limited system (in the sense that aberrations effects are small compared to diffractions effects) as can be seen in the spot diagram in Figure 4.9(a). The telescope introduces no significant aberrations as can be seen in the spot diagram in Figure 4.9(b) and therefore, the phase contrast imaging system is also diffraction limited. The loss in resolution is mainly due to the reduced exit pupil and not to aberrations. The resulting spread functions ($|PSF|^2$) are shown in Figure 4.10 for both optical systems. The distance between the maximum and the first minimum of the spread function commonly defines the incoherent resolution limit (Rayleigh criterion), which is $1.1\,\mu\text{m}$ for the absorption imaging system and $1.4\,\mu\text{m}$ with the telescope.

In practice, we would like to accurately determine the number of atoms in each microscopic cloud. When counting atoms we define a finite region of interest around one cloud and integrate the column density over this region. The accuracy of this method depends on the capability to confine the signal within a small region so that no overlap with the neighbouring clouds occurs.

The spread functions enables one to evaluate how well the imaging system can concentrate, in image space, the collected photons originating from a point source or a cloud. Indeed, integrating the spread functions in space leads to the amount of energy per unit time collected in this region. It is then possible to calculate the fraction of energy collected within a disk centred on the cloud. The results are presented in Figure 4.11. As expected, the phase contrast imaging setup cannot confine the energy as well as the original absorption imaging setup. But for typical

(a) Absorption imaging setup.

(b) Phase contrast imaging setup.
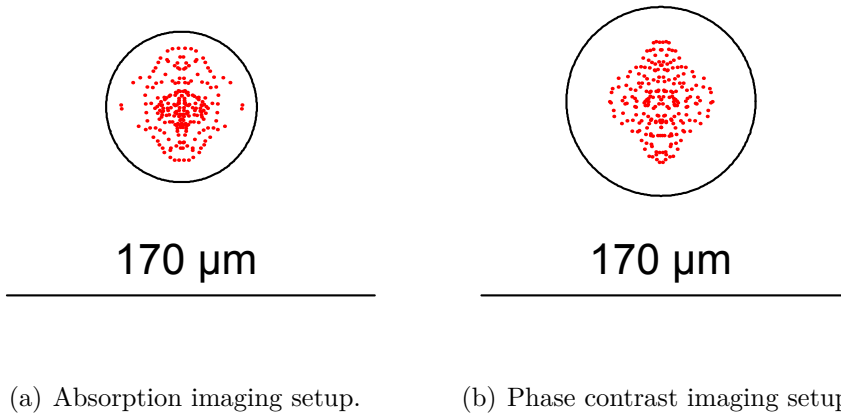
Figure 4.9: Spot diagram for the absorption imaging setup 4.9(a), and for the phase contrast imaging setup 4.9(b) (with telescope). The black circle denotes the size of the Airy disk and the scale ($170\,\mu$m) corresponds to the distance between two adjacent microscopic clouds in image space. Geometrical aberrations, illustrated by the ray impacts, are comparably small for both setups. However, the reduced aperture of the relay telescope enlarges the Airy disk in the case of the phase contrast system.
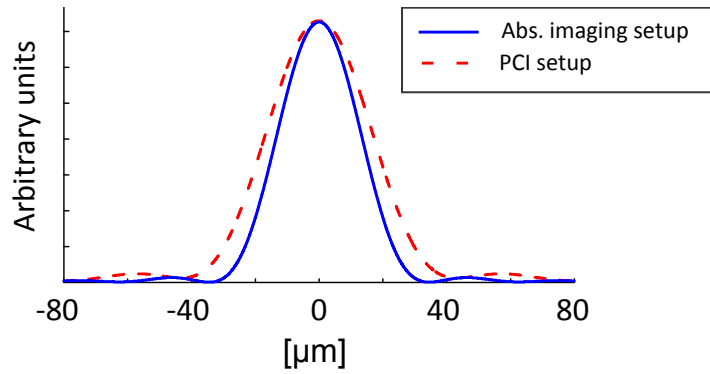
Figure 4.10: Cut of the spread functions ($|PSF|^2$) for the absorption imaging setup and the phase contrast imaging setup. Loss of resolution is illustrated by the extent of the spread function.
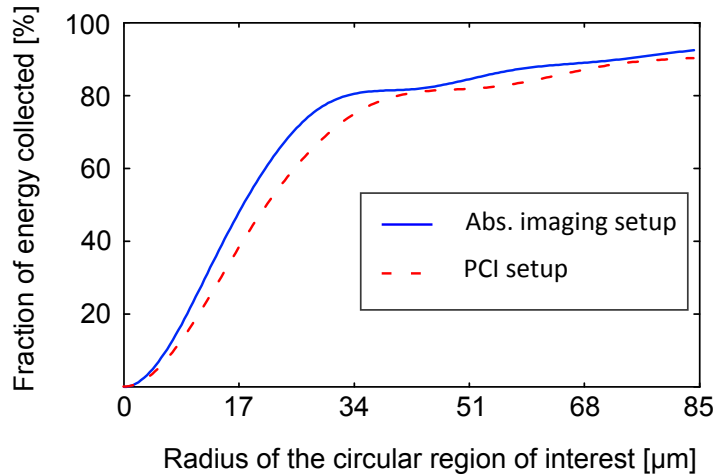
Figure 4.11: Encircled energy for both setups.

regions of interest, with diameter equivalent to the inter-cloud distance, the overall performance is comparable (approximately 90 % of the signal is enclosed by the region).

4.2.4 Tolerancing

The optical performances discussed above are valid only when the optical components are perfectly aligned and centred. We now investigate the case where components are slightly tilted and misaligned in order to identify the sensitive components and design the optomechanics accordingly.

Ideally, our phase contrast imaging system is diffraction limited, which can be expressed quantitatively by comparing our ideal RMS wavefront error ($0.037\,\lambda$) with Maréchal's criterion (RMS wavefront error smaller than $0.07\,\lambda$). In the tolerancing procedure, we search, for each optical component, the maximal displacement (tilt or decentering) until the system does not fulfil Maréchal criterion anymore.

Sometimes, it is possible to compensate the misalignment of one component by moving another one. If one allows for some compensation, tolerances are usually larger.

The tolerances for the telescope are presented in Table 4.2. Additionally, we included the tolerance on the phase plate position. The transversal and axial displacement of the phase plate are limited by the condition that the focused probe beam fits entirely in the phase dip.

The tolerance analysis shows that three degrees of freedom are critical, namely the tilt of each telescope lens and the overall tilt of the telescope.

Degree of freedom	Tolerance without compensation	Tolerance with compensation
Telescope spacing	20 µm	3.5 mm
1st lens decentering	2.5 mm	-
2nd lens decentering	1.4 mm	-
1st lens tilt	0.093°	0.46°
2nd lens tilt	0.093°	0.77°
Telescope decentering	2.9 mm	-
Telescope tilt	0.24°	-
Phase plate axial displacement	±1.5 mm	-
Phase plate lateral displacement	±30 µm	-

Table 4.2: Tolerances for the telescope and the phase plate. If no compensation with an other optical component is needed or possible, cells are kept empty. Tight tolerances are highlighted in red.
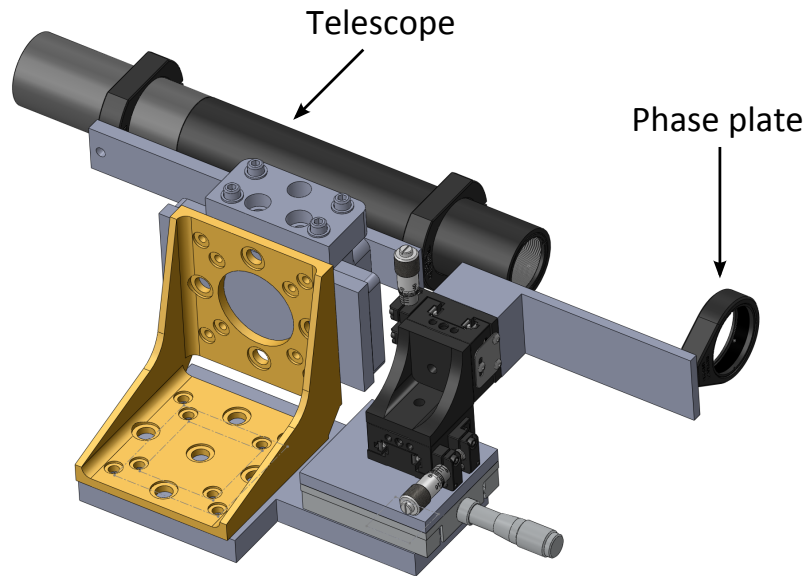
Figure 4.12: Optomechanical system of the phase contrast system.

4.2.5 Optomechanics

The optomechanical system has to be designed in order to fulfil the following two main constraints:

1. The telescope and the phase plate should be able to be moved in and out of the existing absorption imaging setup with high reproducibility.

2. The optomechanics should achieve the required position precision given by the tolerances.

In order to accurately move the phase contrast system, we decided to use a translation stage with micrometer precision and a sufficient travel range of 50 mm (model **VT-80** from **Micos**).

Since the system is quite sensitive to the relative tilt of each telescope lens, we decided to insert the lenses in a rigid tube to ensure the parallelism of the components. The tube support, which defines the overall tilt of the telescope, is a precise tilt aligner from **Newport** (model **9071**). Finally, the phase plate is supported by three micrometer translation stages for the lateral and axial positioning.

The remaining mechanical adapters and holders were made at the workshop of the institute.

The overall optomechanical system is shown in Figure 4.12 where we omit the Micos translation stage and the support base.

4.2.6 Positioning of the phase plate

The precise positioning of the phase plate is a crucial and delicate task. The dip is a sub-wavelength structure and does not scatters light notably compared to any dust particle. It could be therefore misleading to search for the dip by looking at the scattered light of the focused probe beam.

In order to find the dip, we rather build an appropriate pinhole mask (with 1 mm diameter), that we placed against the substrate and centred on the dip. We then aligned approximately the phase plate by focusing the probe beam in the centre of the pinhole and scanned the surrounding region. The best lateral position can be found by either maximising the phase contrast signal or by *sensing* the edges of the circular structure and then centring the phase dip accordingly.

The axial position can also be evaluated with the pinhole mask by estimating the waist of the focused beam through the focus. Experimentally, we observed that an axial displacement of the phase plate introduces an inhomogeneous Gaussian pattern to the originally flat background. We suspect here interference of the probe beam at the dip structure. The best axial position is then found when the background is homogeneous and at the same level as when the probe beam crosses the phase plate outside of the dip.

4.3 Experimental results

4.3.1 First light: Observation of a large BEC

Our first phase contrast images were done with a large BEC containing around 50 000 atoms of ^{87}Rb. The probe beam was red-detuned by approximately 50 MHz ($\delta \approx -16$ in half linewidths) with a probe intensity of $19 \, \text{mW cm}^{-2}$ (11 times the cycling transition saturation intensity) and the exposure time was $15 \, \mu\text{s}$. Phase contrast imaging requires two pictures, namely one picture in the presence of atoms and a second reference picture in the absence of atoms. They are shown in Figure 4.13.

Because of the high column density, the signal shows a periodicity, characteristic of phase contrast imaging. As expected for red-detuned light and a $-\pi/2$ phase plate, the intensity decreases first for the low densities near the edges of the clouds; then the intensity reaches a minimum, grows again and surpasses the background level in the centre of the cloud, where the column density is maximal.

4.3.2 Calibration and quantitative measurements

In order to perform precise quantitative measurements, for example deduce the exact number of atoms in a cloud, we have to calibrate the imaging in order to account for experimental imaging conditions that we earlier ignored for simplicity, such as the linear polarisation of the probe beam, a residual magnetic field or the multilevel structure of the excited state. The experimental imaging beam is then $\pi-$polarised.
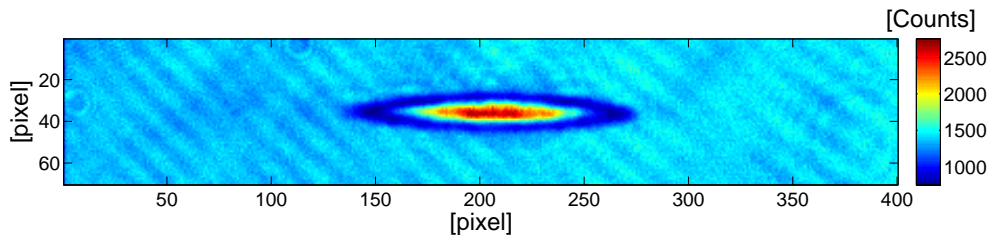
(a) Picture with atoms.
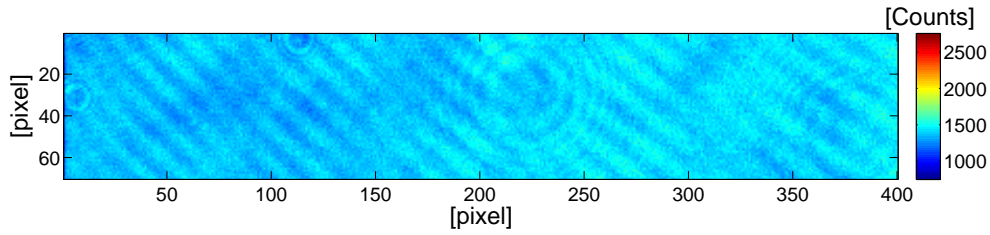
(b) Reference picture.
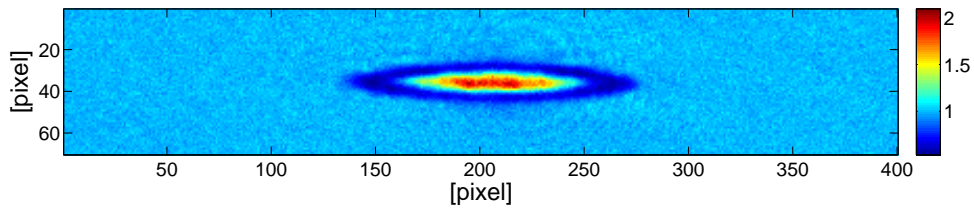
(c) Normalised intensity I_a/I_{ref}.
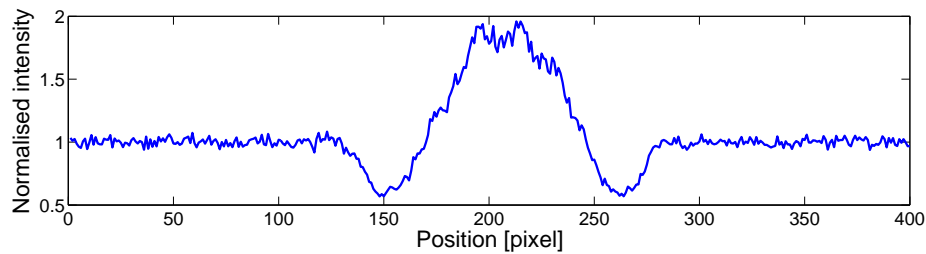
(d) Horizontal cut of the normalised intensity.

Figure 4.13: Phase contrast pictures in the presence of atoms 4.13(a), and in the absence of atoms 4.13(b). The normalised intensity I_a/I_{ref} is shown in 4.13(c) and an horizontal cut at the centre of the cloud is plotted in 4.13(d). The detuning of the probe beam is $\delta \approx -16$ with a saturation parameter around 10. The pixel size is $13\,\mu$m in image space and $0.42\,\mu$m in object space.

Calibration method

The calibration procedure is described in Muessel et al. [15] and relies on the dependence of the *quantum projection noise* over atom number (see Itano et al. [22]). We shall briefly review the method here. We prepare a cloud of independent atoms in an equal superposition of two states $|A\rangle$ and $|B\rangle$ (in our case $|A\rangle$ and $|B\rangle$ are two Zeeman sublevels of the ground state of ^{87}Rb). If the system is well-calibrated, the variance of the measured population difference should be an affine function of the total measured atom number with unit slope. Furthermore, this relation should be independent of the imaging intensity so that we measure two independent conditions and can therefore determine the two calibration parameters that arise for the distinct intensity dependence of the formula

$$n_c = -\frac{1}{\sigma_0}\left[c_1(1+\delta^2)\ln\left(\frac{I_f}{I_{ref}}\right) + \frac{I_f - I_{ref}}{c_2 I_{sat}}\right], \tag{4.4}$$

where c_1 and c_2 are calibration parameters, I_{ref} is the reference intensity and I_f is the intensity right after the cloud. I_f can be numerically deduced from the phase contrast images I_a and I_{ref} by mean of the relation

$$I_a = I_{ref}\left[\frac{I_f}{I_{ref}} + 2 + 2\sqrt{\frac{I_f}{I_{ref}}}\cos\left(\frac{\delta}{2}\ln\frac{I_f}{I_{ref}} - \alpha\right) - 2\sqrt{\frac{I_f}{I_{ref}}}\cos\left(\frac{\delta}{2}\ln\frac{I_f}{I_{ref}}\right) - 2\cos\alpha\right], \tag{4.5}$$

where α is the phase shift of the phase plate. Note that α and δ are considered to be fixed parameters. The exposure time for the calibration, $\tau = 35\,\mu\text{s}$, was chosen to maximise the experimental SNR on phase contrast images for a blue-detuning of $\delta = 3.3$. Note that, as expected theoretically, the optimal exposure time is longer for phase contrast imaging than for absorption imaging ($\tau_{abs} \approx 15\,\mu\text{s}$). The calibration is performed with a set of saturation intensities between 5 and 35 I_{sat} and for several detunings between 1.6 and 8.2 half linewidths.

Calibration attempt

In the following section, we report on the progress concerning the calibration of our phase contrast system. Results presented here are therefore not definitive but rather reflect what we so far achieved in this field.

Our first calibration shows an unexpected detuning dependence: the column density is clearly under-estimated for lower detunings compared to higher detunings. We then restricted our calibration to one detuning, namely the one for which we choose the optimal exposure time, $\delta = 3.3$.

A calibration curve for suitable calibration parameters ($c_1 = 2.3$ and $c_2 = 1$) is shown in Figure 4.15. An other unexpected issue (most likely related to the detuning dependence) is that the calibration parameters found this way for phase contrast imaging differ clearly from absorption imaging parameters ($c_1 = 5.9$ and $c2 = 1.35$)
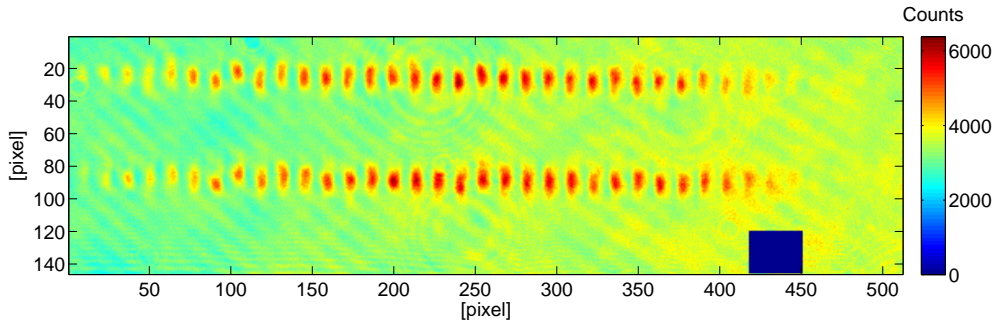
(a) Picture with atoms.
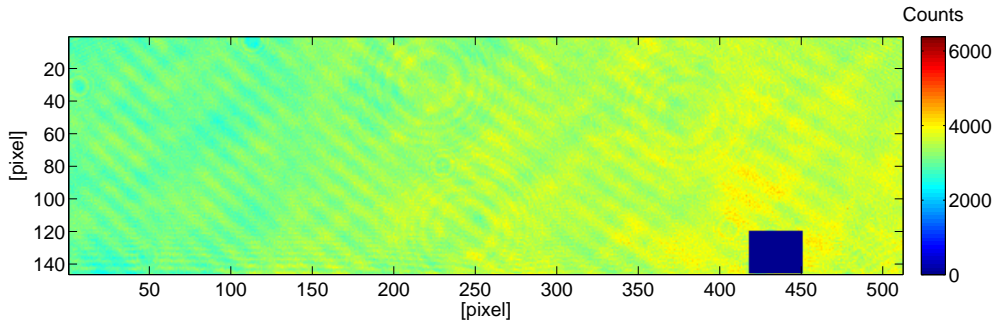


(b) Reference picture.
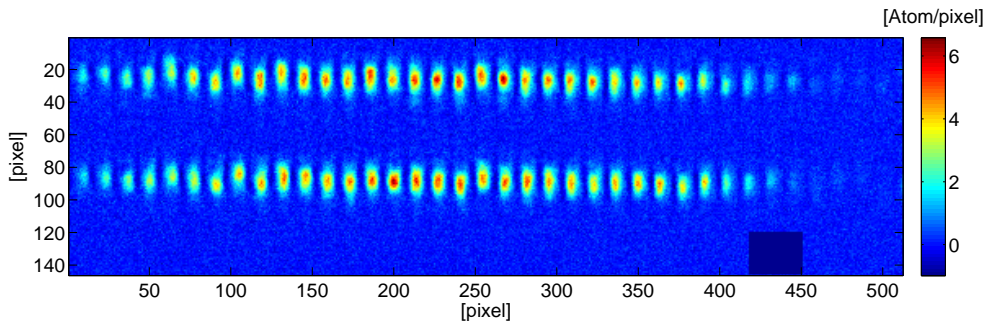
(c) Column density profile.

Figure 4.14: Example of phase contrast images used for the calibration, 4.14(a), 4.14(b) and the deduced column density 4.14(c). Each one-dimensional array corresponds to a Zeeman sublevel of the ground state. The variance in the number of atoms measured in the two components enables the calibration of the imaging setup. The detuning of the probe beam is $\delta \approx 3.3$ with a saturation parameter around 10. As expected from a blue-detuned probe beam, atoms introduce a positive signal. The pixel size is $13\,\mu m$ in image space and corresponds to $0.42\,\mu m$ in object space.
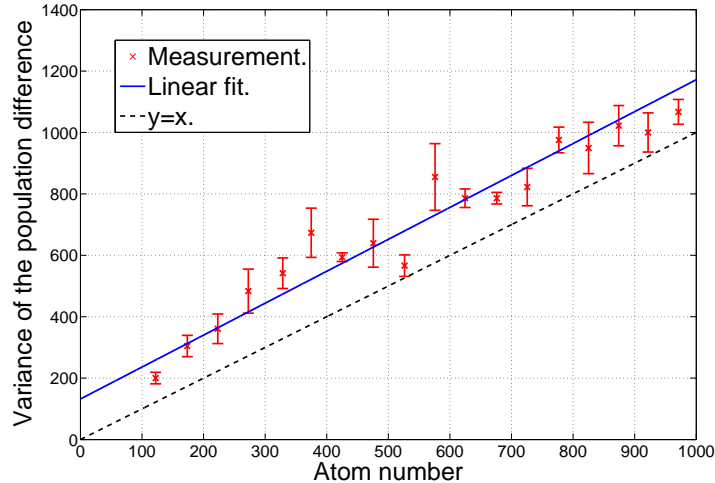
Figure 4.15: Variance of the population difference over atom number for suitable calibration parameters. The detuning is $\delta = 3.3$ and the saturation parameter $s_0 = 35$.

although they should be close. The slope of nearly one demonstrates the success of the calibration for this particular intensity and detuning. The dependence of the calibration slope on the saturation parameter in shown in Figure 4.16. Ideally, the calibration slope is equal to one independent of the probe intensity, which is the case for this calibration.

The detection noise σ_{det}^2, which states the precision of the atom number determination, can be evaluated by the offset of the unity-slope calibration curve in Figure 4.15. In our case, the average detection noise for saturations between $s_0 = 5$ and $s_0 = 35$ is $\sigma_{det}^2 = 100 \pm 20$ at a detuning $\delta = 3.3$. Therefore, the precision on the atom number determination is $\sigma_{det} \approx 10$ atoms, which is comparable to the best resolution obtained with optimised absorption imaging, $\sigma_{det} = 3.7$ atoms.

4.3.3 Limitations

As mentioned earlier, for the calibration to be completely satisfying, one parameter set should be valid for all detunings, which is not the case presently. We list below some practical issues that might be responsible for this discrepancy and also propose some solutions.

As can be seen in the raw pictures in Figure 4.16, images are subject to a relatively strong fringe pattern, mainly originating from the uncoated phase plate and from dust particles. If the fringe pattern is not stable while the atom picture and the reference picture are taken, this introduces *fringe noise* that may be stronger than the shot noise. Furthermore, since fringes are features introduced after the probe beam have passed the atoms, it is, in principle, not correct to interpret the intensity measured without atom I_{ref} to be the probe intensity I_0 as we did in Equations (4.4)
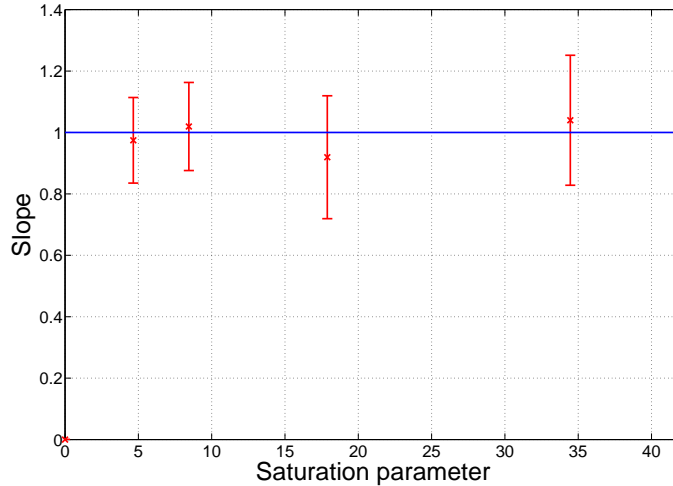
Figure 4.16: Slope of the calibration curve for different saturation parameters and for a detuning $\delta = 3.3$.

and (4.5). These issues can be addressed practically by coating the flat surface of the phase plate or by additional post-processing of the image.

We experimentally observe that phase contrast images are more subject to interferences between clouds than absorption images. For example, it exhibits stronger *undershoots* between adjacent clouds. Since *undershoots* are not related to the phase contrast signal, they have to be dealt with, for example by choosing a region of interest that excludes *undershoots* or by practically increasing the inter-well distance.

All calibration measurements were performed with the same exposure time of 35 μs, which seemed to be near-optimal for a detuning $\delta = 3.3$. As seen in Section 3.2, for each detuning there is a corresponding optimal exposure time. If the exposure time is too long, no useful signal is collected in the last stage of the exposure and the inferred intensity I_a is underestimated compared to the intensity that would be measured with an optimal exposure time. This could be the reason for the detuning dependence we observed in our calibration and, in particular, explain why the measured column density grows with the detuning.

5 Conclusion

During this master thesis, we investigated theoretically and implemented an imaging technique – phase contrast imaging – to provide a new tool with which to probe Bose-Einstein condensates in our lab. We started by investigating the existing absorption imaging technique and compared it with phase contrast imaging on a theoretical basis. Although the comparison is well documented when phase contrast is performed with high detuning, the performance of near-resonant phase contrast imaging is rather unknown and we have explored this new regime.

Theoretically, we found that near resonant phase contrast imaging should deliver a better signal-to-noise ratio than absorption imaging for typical experimental saturations and for the cycling transition of ^{87}Rb. This results from the combination of a stronger signal and the possibility to expose longer. Near-resonant phase contrast as well as absorption imaging are destructive techniques that lead to a rapid expansion of the imaged cloud during exposure time. We developed a simple model to describe the imaging of an expanding cloud that helped us to understand the imaging process better, especially the limitation on the exposure time. In order to cross-check our theoretical investigations and to investigate further practical issues, we numerically simulated phase contrast and absorption imaging systems.

The last part of this thesis was dedicated to the design and implementation of the optical system. The most crucial component, the phase plate, was designed according to the existing system, fabricated outside of the institute and finally characterised with interferometric methods. We implemented phase contrast imaging as a flexible tool that can be moved in and out of the existing imaging setup so that both techniques (absorption and phase contrast imaging) are available within a few seconds. We finally reported on the on-going attempt to reach a complete and valid calibration of our phase contrast system and discussed the actual limitations.

Although we considered in this thesis only the case of near-resonant phase contrast imaging, nothing prevents our setup to be used in the more usual way, with larger detuning and as a non-destructive technique.

Our phase contrast imaging setup does not yet perform in its maximal capability but there is good hope that once optimised, this technique becomes a valid alternative to absorption imaging, even for relatively thin clouds.

6 Appendix

A Phase contrast imaging theory

A.1 Two-lens imaging

Let f, g and h be the complex amplitudes in the object plane $(x - y)$, Fourier plane $(\xi - \eta)$, and image plane $(x' - y')$ respectively, as shown in Figure A.1. The Fourier property of a lens leads to

$$g(\xi, \eta) = C_1 \mathcal{F}[f(x, y)] \left(\frac{\xi}{\lambda f_1}, \frac{\eta}{\lambda f_1} \right) \tag{A.1}$$

with $C_1 = \frac{\mathrm{i}}{\lambda f_1} \mathrm{e}^{-2\mathrm{i}k f_1}$, and

$$h(x', y') = C_2 C_3 \mathcal{F}[g(\xi, \eta)] \left(\frac{x'}{\lambda f_2}, \frac{y'}{\lambda f_2} \right), \tag{A.2}$$

with $C_2 = \frac{\mathrm{i}}{\lambda f_2} \mathrm{e}^{-\mathrm{i}k(f_2 + d)}$, and $C_3 = \mathrm{e}^{\mathrm{i}\pi \frac{(x'^2 + y'^2)(d - f_2)}{\lambda f_2}}$. Substitution of (A.1) into (A.2) gives

$$h(x', y') = C \iint_{-\infty}^{+\infty} \left[\iint_{-\infty}^{+\infty} f(x, y) \, \mathrm{e}^{-2\mathrm{i}\pi(\frac{\xi}{\lambda f_1}x + \frac{\eta}{\lambda f_1}y)} \, \mathrm{d}x \, \mathrm{d}y \right] \mathrm{e}^{-2\mathrm{i}\pi(\frac{x'}{\lambda f_2}\xi + \frac{y'}{\lambda f_2}\eta)} \, \mathrm{d}\xi \, \mathrm{d}\eta$$

$$= C \iiiint_{-\infty}^{+\infty} f(x, y) \, \mathrm{e}^{-2\mathrm{i}\pi\xi(\frac{x}{\lambda f_1} + \frac{x'}{\lambda f_2})} \, \mathrm{e}^{-2\mathrm{i}\pi\eta(\frac{y}{\lambda f_1} + \frac{y}{\lambda f_2})} \, \mathrm{d}x \, \mathrm{d}y \, \mathrm{d}\xi \, \mathrm{d}\eta, \tag{A.3}$$

with $C = C_1 C_2 C_3$.

Using the transformation $u = \frac{2\pi\xi}{\lambda f_1}$ and $v = \frac{2\pi\eta}{\lambda f_1}$, one gets,

$$h(x', y') = C \left(\frac{\lambda f_1}{2\pi} \right)^2 \int_{-\infty}^{+\infty} \mathrm{d}u \int_{-\infty}^{+\infty} \mathrm{d}v \iint_{-\infty}^{+\infty} f(x, y) \, \mathrm{e}^{-\mathrm{i}u(x - \frac{x'}{M})} \, \mathrm{e}^{-\mathrm{i}v(y - \frac{y'}{M})} \, \mathrm{d}x \, \mathrm{d}y, \tag{A.4}$$

with $M = -\frac{f_2}{f_1}$ the magnification (the minus sign meaning that the image is inverted). Finally, we obtain, by the application of the Fourier integral theorem[1], the

---

[1] If $f(x, y)$ is a complex piecewise smooth function and $\iint_{-\infty}^{\infty} |f(x, y)| \, \mathrm{d}x \, \mathrm{d}y$ exists (for more details, see Courant and Hilbert [23]), then:

$$f(x, y) = \frac{1}{(2\pi)^2} \int_{-\infty}^{+\infty} \mathrm{d}u \int_{-\infty}^{+\infty} \mathrm{d}v \iint_{-\infty}^{+\infty} f(t, s) \, \mathrm{e}^{-\mathrm{i}u(t - x)} \, \mathrm{e}^{-\mathrm{i}v(s - y)} \, \mathrm{d}t \, \mathrm{d}s.$$

In practice, smoothness and integrability are always fulfilled by real complex amplitudes.
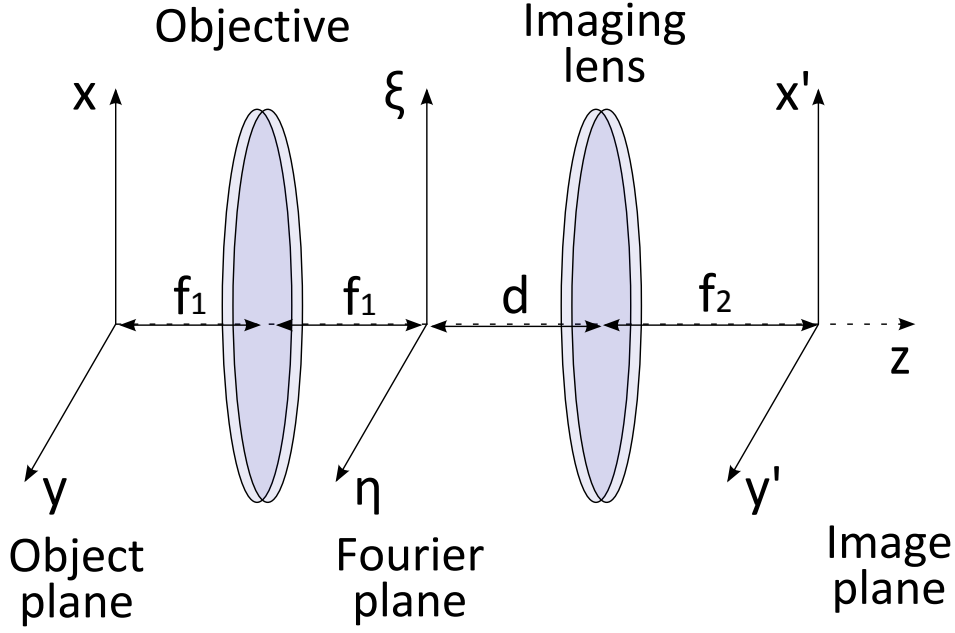
Figure A.1: Schematic representation of the imaging setup.

complex amplitude in the image plane,

$$h(x', y') = C\lambda^2 f_1^2\ f\left(\frac{x'}{M}, \frac{y'}{M}\right),$$ (A.5)

and the intensity in the image plane,

$$\begin{aligned}
I(x', y') &= |h(x', y')|^2, \\
&= \left(\frac{f_1}{f_2}\right)^2\ \left|f\left(\frac{x'}{M}, \frac{y'}{M})\right)\right|^2, \\
&= \frac{1}{M^2}\ I_f\left(\frac{x'}{M}, \frac{y'}{M}\right),
\end{aligned}$$ (A.6)

where $I_f = |f|^2$ is the intensity in the object plane. The image is then a **perfect**, scaled replica of the object. Nevertheless, in reality (even with perfect optics) the image is a **blurred** replica of the object because of the finite aperture of our system. The real image is not obtained with the complex amplitude (A.5) but with the real complex amplitude, which is the convolution of (A.5) with the point spread function $(\text{PSF}(x, y))$ of the imaging system,

$$h_{real}(x', y') = C\lambda^2 f_1^2\ \left[f\left(\frac{x'}{M}, \frac{y'}{M}\right) * \text{PSF}(x', y')\right],$$ (A.7)

where $*$ represents the two-dimensional convolution.

A.2 Ideal phase contrast imaging

Let us now consider the case of phase contrast imaging where the zero-order diffracted wave is phase shifted in the Fourier plane by a phase α. Being able to phase shift exclusively the zero order wave without disturbing the diffracted wave is an **idealization** that we are going to consider in the section A.3.

A.2.1 Intensity in the image plane as function of the atom phase shift

Using the superposition principle, we can write the complex amplitude in the object plane (which is the plane just after the object) as the sum of two other complex amplitudes, which we will identify as the undiffracted (zero-order) and the diffracted waves,

$$f(x,y) = f_0(x,y) + f_d(x,y), \tag{A.8}$$

with $f_0(x,y)$ the complex amplitude that would be obtained if no object were present. If the thickness of the object is small compared to the variation of the complex envelope of the probe wave along the z-axis, $f_0(x,y)$ can be seen as the complex amplitude just before the object, so that the complex amplitude after transmission through the object can be written as,

$$f(x,y) = f_0(x,y) \ t(x,y) \ e^{i\phi(x,y)} \tag{A.9}$$

with $t(x,y)$ the transmission coefficient and $\phi(x,y)$ the phase shift introduced by the object. From (A.8) and (A.9), one find the expression for the diffracted complex amplitude,

$$f_d(x,y) = f_0 \left[t(x,y) \ e^{i\phi(x,y)} - 1 \right]. \tag{A.10}$$

Using the Fourier transform property of the objective, the complex amplitude in the Fourier plane can also be expressed as a sum,

$$g(\xi,\eta) = C_1 \left[g_0(\xi,\eta) + g_d(\xi,\eta) \right], \tag{A.11}$$

with g_0 and g_d the Fourier transform of f_0 and f_d respectively evaluated in $\frac{\xi}{\lambda f_1}$ and $\frac{\eta}{\lambda f_1}$.

In practice, f_0 has very low spatial frequencies compared to the diffracted wave. In the idealised case where the probe wave is a plane wave, $f_0 = \sqrt{I_0}$ is a constant (I_0 beeing the probe beam intensity). Diffracted and undiffracted waves are then well-separated in the Fourier plane and g_0 reduces to a Dirac delta for an incident plane wave.

Until now, we have just used the superposition principle to rewrite the amplitude in the Fourier plane (A.1) in a convenient way. It is now possible to apply a phase

shift to the undiffracted wave by multiplying the "zero order" complex amplitude by the factor $\tau e^{i\alpha}$ so that the complex amplitude after the phase plate is given by[2]

$$g'(\xi, \eta) = C_1 \left[\tau e^{i\alpha} g_0(\xi, \eta) + t_s \ g_d(\xi, \eta) \right], \tag{A.12}$$

where τ is the transmission coefficient of the phase dip, α the phase shift introduced by the phase plate[3] and t_s is the transmission coefficient of the phase plate substrate. In most of the cases, $\tau = t_s$ because the dip is dug in the substrate. Nevertheless, the raw contrast can be enhanced using more elaborated phase plates where $\tau < t_s$.

Performing another Fourier transformation and using the Fourier integral theorem yield to the complex amplitude in the image plane,

$$\begin{aligned}
h(x', y') &= C_2 C_3 \ \mathcal{F}[g'(\xi, \eta)] \left(\frac{x'}{\lambda f_2}, \frac{y'}{\lambda f_2} \right), \\
&= C \ \mathcal{F} \left[\tau e^{i\alpha} g_0(\xi, \eta) + t_s \ g_d(\xi, \eta) \right] \left(\frac{x'}{\lambda f_2}, \frac{y'}{\lambda f_2} \right), \\
&= C \ \lambda^2 f_1^2 \ \left[\tau e^{i\alpha} \ f_0 \left(\frac{x'}{M}, \frac{y'}{M} \right) + t_s \ f_d \left(\frac{x'}{M}, \frac{y'}{M} \right) \right].
\end{aligned} \tag{A.13}$$

The intensity in the image plane for phase contrast imaging is

$$\begin{aligned}
I(x', y') &= |h(x', y')|^2 = |C\lambda^2 f_1^2|^2 \ |f_0 \left(\frac{x'}{M}, \frac{y'}{M} \right) \ (\tau e^{i\alpha} + t_s \ t \left(\frac{x'}{M}, \frac{y'}{M} \right) \ e^{i\phi(\frac{x'}{M}, \frac{y'}{M})} - t_s)|^2 \\
&= \frac{I_0 \left(\frac{x'}{M}, \frac{y'}{M} \right)}{M^2} \ |\tau e^{i\alpha} + t_s \ t \left(\frac{x'}{M}, \frac{y'}{M} \right) \ e^{i\phi(\frac{x'}{M}, \frac{y'}{M})} - t_s|^2.
\end{aligned} \tag{A.14}$$

Omitting the variables for better visibility, one gets

$$I = \frac{I_0}{M^2} \left[t_s^2 t^2 + t_s^2 + \tau^2 + 2t_s t\tau \cos(\phi - \alpha) - 2t_s^2 t \cos\phi - 2t_s\tau \cos\alpha \right] \tag{A.15}$$

The intensity (A.15) is the general expression for a 2-lens imaging system with a phase plate in the Fourier plane. Standard phase contrast imaging is obtained as a special case where $\alpha = \pm\frac{\pi}{2}$ and $\tau = t_s = 1$,

$$I(x', y') = \frac{I_0}{M^2} \left[2 + t^2 \pm 2t \sin(\phi) - 2t \cos\phi \right] \tag{A.16}$$

and reduces for small ϕ and for a phase object ($t = 1$) to

$$I(x', y') = \frac{I_0}{M^2} \left[1 \pm 2\phi \right]. \tag{A.17}$$

---

[2] We neglected here the depth of the dimple since it is of the order of a half-wavelength compared to the depth of focus of the probe beam on the order of a few hundreds micrometer.

[3] A positive phase shift ($\alpha > 0$) means that the phase of the "zero order" is retarded compared to the diffracted wave. Negative α corresponds to an advance of the "zero order".

Phase contrast imaging can also be advantageously performed using a non-transparent phase dip ($\tau < t_s = 1$). If the object is transparent ($t = 1$),

$$I(x', y') = \frac{I_0}{M^2} \left[2 + \tau^2 \pm 2\tau \sin(\phi) - 2\cos\phi \right] \tag{A.18}$$

and reduces for small ϕ to

$$I(x', y') = \frac{I_0}{M^2} \left[\tau^2 \pm 2\tau\phi \right]. \tag{A.19}$$

Absorption imaging is obtained in the absence of phase plate ($\alpha = 0$, $t_s = \tau = 1$), with resonant probe light ($\phi = 0$), and expression (A.15) reduces to (A.6),

$$I(x', y') = \frac{I_0}{M^2} \, t^2 = \frac{I_f}{M^2}. \tag{A.20}$$

A.3 Effect of the size of the phase dip

In the previous derivation, we idealised the action of the phase dip in applying a phase shift only to the undiffracted wave and nothing to the diffracted wave. In practice the phase shift is introduced by a phase dip with a given size so that his effect differs from the idealisation by two ways:

1. First, a small part of the diffracted wave will still cross the phase dip and experience an undesired phase shift.

2. Second, the undiffracted wave that focus in the middle of the phase dip has in fact an infinite spatial extension so that a small part (the wings) of the zero order will cross the Fourier plane outside of the phase dip.

A.3.1 Effect of the spatial extension of the focused probe beam

In opposition to perfect geometrical systems, that can focus a beam into a point, diffraction and optical aberrations leads to smeared focus. If the size of the spot exceeds the size of the phase dip or in case of misalignment, a non negligible part of the undiffracted wave miss the phase dip and does not experience the crucial phase shift. It is possible to qualitatively describe this effect by considering the interference of three waves in the image plane:

- the diffracted wave: f_d,

- the part of the undiffracted wave that crossed the phase dip: $p \, f_0 \, e^{i\alpha}$,

- and the rest part that did not pass through the dip: $(1 - p) f_0$,

where p the fraction of amplitude of the undiffracted wave that crosses the dip.

In the image plane the intensity is given by:

$$I \propto |f_d + \mathrm{p} \; f_0 \; \mathrm{e}^{\mathrm{i}\alpha} + (1 - \mathrm{p})f_0|^2 \tag{A.21}$$

Using the relation: $f_d = f_0(t\mathrm{e}^{\mathrm{i}\phi} - 1)$, one finds:

$$I \propto I_0 \left[t^2 + 2\mathrm{p}t\cos(\phi - \alpha) - 2\mathrm{p}t\cos\phi + 2\mathrm{p}^2 - 2\mathrm{p}^2\cos\alpha \right]. \tag{A.22}$$

In the case of standard phase contrast imaging $(\alpha \pm \frac{\pi}{2})$ and for small ϕ, the intensity is an affine function of the phase,

$$I \propto I_0 \left[1 + 2\mathrm{p}^2 - 2\mathrm{p} \pm 2\mathrm{p}\phi \right]. \tag{A.23}$$

If the phase dip has an equivalent size than the focused probe beam (p<1), it leads to a lower background and a lower phase sensitivity. For example, for p = 1/2,

$$I \propto I_0 \left(\frac{1}{2} \pm \phi \right).$$

A.3.2 Effect of the size of the dip with respect to the diffracted wave

The phase dip being not infinitely small, a small fraction of the diffracted wave also crosses the phase dip and causes therefore no useful signal. It is possible by means of Fourier optics considerations to understand how the image is influence by the phase dip : The objective maps in the Fourier plane the multiple frequencies comprises in the object plane amplitude. The phase dip acts therefore in the frequency domain as an exclusion filter for the phase signal frequencies. Namely the spatial frequencies mapped on the phase dip will remain invisible. If the phase dip is centred on the optical axis, it acts as a low pass filter with cut-off frequency: $|\nu_c| = \frac{d/2}{\lambda f}$, where d is the dip diameter, f the objective focal length and λ the wavelength. Big phase structures are not well reproduced and their edges appears much more pronounced.

A.3.3 Rigorous treatment

In order to take into account the real size of the phase dip as well as the spatial extension of the focused probe beam, we introduce the transmission function of the Zernike plate (N'Diaye et al. [24]),

$$t_Z(\xi, \eta) = 1 + (\tau\mathrm{e}^{\mathrm{i}\alpha} - 1)Z(\xi, \eta), \tag{A.24}$$

where τ is the transmission coefficient of the phase dip, α the dip phase shift and Z the shape of the phase dip [4]. In our case, the phase dip is circular so that

$$Z(\xi, \eta) = \begin{cases} 1 & \text{if } \sqrt{\xi^2 + \eta^2} \leq r \\ 0 & \text{otherwise,} \end{cases} \tag{A.25}$$

with $2r$ the diameter of the phase dip. If $g(\xi, \eta)$ is the complex amplitude just before the Zernike plate, we can write the amplitude just after the phase dip,

$$\begin{aligned} g'(\xi, \eta) &= t_Z \, g(\xi, \eta), \\ &= \left[1 + (\mathrm{e}^{\mathrm{i}\alpha} - 1)Z(\xi, \eta) \right] g(\xi, \eta). \end{aligned} \tag{A.26}$$

The amplitude in the image plane is

$$\begin{aligned} h(x', y') &= C_2 C_3 \, \mathcal{F}[g'(\xi, \eta)] \left(\frac{x'}{\lambda f_2}, \frac{y'}{\lambda f_2} \right), \\ &= C \iint_{-\infty}^{+\infty} t_Z \left[\iint_{-\infty}^{+\infty} f(x, y) \, \mathrm{e}^{-2\mathrm{i}\pi(\frac{\xi}{\lambda f_1}x + \frac{\eta}{\lambda f_1}y)} \, \mathrm{d}x \, \mathrm{d}y \right] \mathrm{e}^{-2\mathrm{i}\pi(\frac{x'}{\lambda f_2}\xi + \frac{y'}{\lambda f_2}\eta)} \, \mathrm{d}\xi \, \mathrm{d}\eta. \end{aligned} \tag{A.27}$$

Solutions for this two successive Fourier transformations can be found in Beyer [25] in the case of simple phase object structure and circular phase dip and in Matthews [26] for a Gaussian probe beam in one dimension.

A.4 Shot-noise limited Signal to Noise Ratio

Let N_b and N_s be the number of counts due to Background and signal on the imaging detector, respectively. Using (A.19), one have

$$\begin{aligned} N_s &\propto \tau^2 \pm 2\tau\phi, \\ N_b &\propto \tau^2, \end{aligned} \tag{A.28}$$

The signal is given by

$$S = |N_s - N_b| \propto 2\tau|\phi|. \tag{A.29}$$

In the shot noise limited case, the variance are $\sigma_b^2 = N_b$ and $\sigma_s^2 = N_s$. The noise is then given by

$$\begin{aligned} N = \sqrt{\sigma_b^2 + \sigma_s^2} &\propto \sqrt{2\tau^2 \pm 2\tau\phi}, \\ &\propto \sqrt{2\tau}\sqrt{\tau \pm \phi}. \end{aligned} \tag{A.30}$$

---

[4]To be rigorous, one should take into account the transmission of the substrate t_s,

$$t_Z(\xi, \eta) = t_s + (\tau \mathrm{e}^{\mathrm{i}\alpha} - t_s)Z(\xi, \eta).$$

The signal to noise ratio is finally given by

$$SNR = \frac{S}{N} \propto \frac{\sqrt{2\tau}\ |\phi|}{\sqrt{\tau \pm \phi}}, \tag{A.31}$$

In the case where $\phi \ll \tau < 1$, the SNR is independent of τ,

$$SNR \propto \sqrt{2}|\phi|. \tag{A.32}$$

The proportionality factor of equation (A.31) is for a digital camera

$$\sqrt{QE_{opt}\ \frac{I_0}{M^2\ h\nu}\ QE_{cam}\ g\ A_{pix}\ t_{exp}},$$

where QE_{opt} is the optical system quantum efficiency, I_0 the probe intensity, M the Magnification, h the Planck's constant, ν the probe frequency, QE_{cam} the camera quantum efficiency, g the camera gain, A_{pix} the pixel area and t_{exp} the exposure time. So that (A.31) can be exactly written as

$$SNR = \sqrt{QE_{opt}\ \frac{I_0}{M^2\ h\nu}\ QE_{cam}\ g\ A_{pix}\ t_{exp}} \frac{\sqrt{2\tau}\ |\phi|}{\sqrt{\tau \pm \phi}}. \tag{A.33}$$

As can be seen from (A.19) and (A.31), some inconsistencies arises when $\tau \approx \phi$, for example the intensity could become negative and the SNR imaginary. A more careful study where quadratic terms of the phase expansion are taken into account leads to the result

$$SNR \propto \frac{|\phi^2 \pm 2\tau\phi|}{\sqrt{\phi^2 \pm 2\tau\phi + 2\tau^2}}. \tag{A.34}$$

B Specifications sent to Holoeye

B.1 Context

We would like to implement phase contrast imaging to the existing [87]Rubidium BEC experiment. This requires the fabrication of a circular Zernike phase plate for the working wavelength of 780.24 nm.

B.2 Specifications

B.2.1 Substrate (provided by us)

The substrate is an uncoated fused silica window from Newport (reference: FSW16) with main characteristics listed below:

- Diameter $= 30 \, \mathrm{mm} + 0/ - 0.2$ mm.

- Thickness $= 4 \pm 0.1 \, \mathrm{mm}$.

- Refractive index $= 1.453\,67$ at 780.24 nm.

B.2.2 Phase plate structure

The Zernike phase plate consists of a centered circular dip on one of the substrate face (see figure B.1) with characteristics:

- Diameter $= 100 \, \mu\mathrm{m}$.

- Diameter tolerance $= +5/ - 20$ µm.

- Ideal depth $= \frac{\lambda}{4(n-1)} = 430 \, \mathrm{nm}$.

- Depth tolerance $= +30/ - 30$ nm.

- Centering of the dip $< 100 \, \mu\mathrm{m}$.

- Roughness over the etched area (dip) $< 5 \, \mathrm{nm}$.

- Transition zone $< 5 \, \mu\mathrm{m}$.
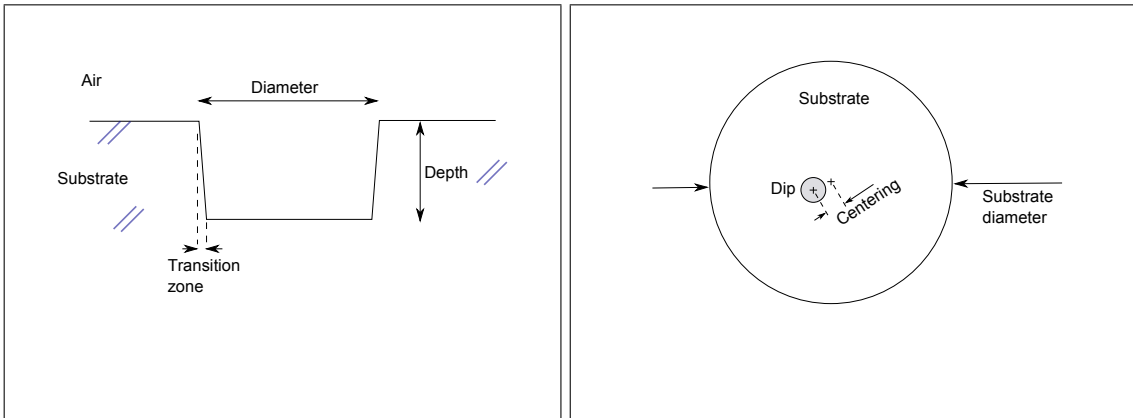
Figure B.1: Phase plate Specifications

C Lists

C.1 List of Figures

C.2 List of Tables

D Bibliography

[1] Erik W. Streed, Andreas Jechow, Benjamin G. Norton, and David Kielpinski. Absorption imaging of a single atom. *Nature Communications*, 3, 2012. URL http://dx.doi.org/10.1038/ncomms1944.

[2] C. Gross, T. Zibold, E. Nicklas, J. Estève, and M. K. Oberthaler. Nonlinear atom interferometer surpasses classical precision limit. *Nature*, 464:pp.1165–1169, Apr 2010. URL http://dx.doi.org/10.1038/nature08919.

[3] B.E.A Saleh and M.C. Teich. *Fundamentals of Photonics*. John Wiley & Sons, 3rd edition, 2007.

[4] Joseph W. Goodman. *Introduction to Fourier Optics*. Roberts & Company Publishers, 3rd edition, 2005.

[5] Max Born and Emil Wolf. *Principles of Optics*. Cambridge University Press, 7th(expanded) edition, 2006.

[6] Pierre Meystre and Murray Sargent III. *Elements of Quantum Optics*. Springer, fourth edition, 2007.

[7] Rudolf Grimm, Matthias Weidemüller, and Yurii B. Ovchinnikov. Optical dipole traps for neutral atoms. volume 42 of *Advances In Atomic, Molecular, and Optical Physics*, pages 95 – 170. Academic Press, 2000. doi: 10.1016/S1049-250X(08)60186-X. URL http://www.sciencedirect.com/science/article/pii/S1049250X0860186X.

[8] R. Meppelink, R. A. Rozendaal, S. B. Koller, J. M. Vogels, and P. van der Straten. Thermodynamics of bose-einstein-condensed clouds using phase-contrast imaging. *Phys. Rev. A*, 81:053632, May 2010. doi: 10.1103/PhysRevA.81.053632. URL http://link.aps.org/doi/10.1103/PhysRevA.81.053632.

[9] John David Jackson. *Classical Electrodynamics*. John Wiley & Sons, 1967.

[10] W. Ketterle, D.S. Durfee, and D.M Stamper-Kurn. Making, probing and understanding bose-einstein condensates. *Proceedings of the Enrico Fermi Summer school, July 1998, Varenna, Italy*, 140:pp.67–164, 1999.

[11] Rodney Loudon. *The Quantum Theory of Light*. Oxford University Press, third edition, 2000.

[12] Daniel Adam Steck. Rubidium 87 d line data. *Journal of Geophysical Research*, 2009(2):31, 2010. URL http://steck.us/alkalidata.

[13] G. Reinaudi, T. Lahaye, Z. Wang, and D. Guéry-Odelin. Strong saturation absorption imaging of dense clouds of ultracold atoms. *Opt. Lett.*, 32(21): 3143–3145, Nov 2007. doi: 10.1364/OL.32.003143. URL http://ol.osa.org/abstract.cfm?URI=ol-32-21-3143.

[14] Frits Zernike. Das phasenkontrastverfahren bei der mikroskopischen beobachtung. *Zeitschrift für technische Physik*, 16:454–457, 1935.

[15] Wolfgang Muessel, Helmut Strobel, Maxime Joos, Eike Nicklas, Ion Stroescu, Jiří Tomkovič, David B. Hume, and Markus K. Oberthaler. Optimized absorption imaging of mesoscopic atomic clouds. *Not yet published*, 2013.

[16] Michael A. Joffe, Wolfgang Ketterle, Alex Martin, and David E. Pritchard. Transverse cooling and deflection of an atomic beam inside a zeeman slower. *J. Opt. Soc. Am. B*, 10(12):2257–2262, Dec 1993. doi: 10.1364/JOSAB.10.002257. URL http://josab.osa.org/abstract.cfm?URI=josab-10-12-2257.

[17] Lev Pitaevskii and Sandro Stringari. *Bose-Einstein Condensation.* Oxford University Press, 2003.

[18] Lorraine Elizabeth Sadler. *Dynamics of a Spin 1 Ferromagnetic Condensate.* PhD thesis, University of California, Berkeley, 2006.

[19] Paul C. Haljan. *Vortices in a Bose-Einstein Condensate.* PhD thesis, University of Colorado, 2003.

[20] Frits Zernike. How i discovered phase contrast. *Nobel lecture.*, 1953.

[21] Timo Ottenstein. A new objective for high resolution imaging of bose-einstein condensates. Master's thesis, University of Heidelberg, 2006. URL http://www.kip.uni-heidelberg.de/matterwaveoptics/publications/theses/diplom_ottenstein.pdf.

[22] W. M. Itano, J. C. Bergquist, J. J. Bollinger, J. M. Gilligan, D. J. Heinzen, F. L. Moore, M. G. Raizen, and D. J. Wineland. Quantum projection noise: Population fluctuations in two-level systems. *Phys. Rev. A*, 47:3554–3570, May 1993. doi: 10.1103/PhysRevA.47.3554. URL http://link.aps.org/doi/10.1103/PhysRevA.47.3554.

[23] R. Courant and D. Hilbert. *Methoden der mathematischen Physik 1.* Verlag von Julius Springer in Berlin, 1924.

[24] Mamadou N'Diaye, Kjetil Dohlen, Thierry Fusco, Kacem El Hadi, Rémi Soummer, Salvador Cuevas, Myriam Zerrad, and Marc Ferrari. Lab results of the circular phase mask concepts for high-contrast imaging of exoplanets. pages 84500N–84500N–9, 2012. doi: 10.1117/12.926876. URL +http://dx.doi.org/10.1117/12.926876.

[25] H. Beyer. *Theorie und praxis des Phasenkontrastverfahren.* Akademische Verlagsgesellschaft, Frankfurt am Main, 1965.

[26] Michael Robin Matthews. *Two-Component Bose-Einstein Condensation.* PhD thesis, University of Colorado, 1999.

Erklärung:

Ich versichere, dass ich diese Arbeit selbstständig verfasst habe und keine anderen als die angegebenen Quellen und Hilfsmittel benutzt habe.

Heidelberg, den (Datum)   . . . .